

# Impact of Josephson Junction Array modes on Fluxonium Readout

Shraddha Singh<sup>1,2,3,\*</sup> Emma Rosenfeld<sup>3,†</sup> Gil Refael<sup>4,3</sup> and Aashish Clerk<sup>5,3</sup>

<sup>1</sup>*Department of Applied Physics and Physics, Yale University, New Haven, Connecticut 06511, USA*

<sup>2</sup>*Yale Quantum Institute, Yale University, New Haven, Connecticut 06511, USA*

<sup>3</sup>*Amazon Web Services, Pasadena 91001, California, USA*

<sup>4</sup>*California Institute of Technology, Pasadena 91001, California, USA*

<sup>5</sup>*University of Chicago, Illinois, USA*

(Dated: September 24, 2024)

Fluxonium qubits, known for their high coherence and fast gates, are a promising candidate for superconducting architectures. High-fidelity measurement of these qubits is a crucial component in employing a fluxonium-based architecture for fault-tolerant quantum computing. We present an analysis of dispersive readout in fluxonium qubits, specifically considering the ‘parasitic’ internal modes of a Josephson junction array (JJA) which constitutes the inductive shunt in the circuit. Measurement of superconducting circuits is currently limited by state transitions in the qubit, when increasing photons in the readout mode, also known as measurement-induced state transitions (MIST). Our analysis reveals that coupling to the parasitic modes of JJA introduces additional state transitions during fluxonium readout. Consequently, such parasitic-mode-assisted MIST effects, which we refer to as p-MIST, can lower the onset of MIST effects to as low as  $\sim 10$  average photons in the readout mode, severely impacting the readout performance. We verify that a significant number of these parasitic transitions, mediated by the coupling of the parasitic mode to the qubit mode, occur with considerable rates. The residual population in the parasitic modes from p-MIST also causes significant dephasing of the fluxonium qubit. We extend our findings across various fluxonium circuits, analyzing the dependency of qubit-parasitic mode coupling on different circuit parameters. Our results underscore the substantial impact parasitic modes can have on the readout fidelity and coherence of highly anharmonic superconducting circuits.

## I. INTRODUCTION

The fluxonium circuit, a Josephson junction shunted by an inductor and a capacitor, is a promising qubit due to its large anharmonicity, flexible parameters, and long lifetimes [1–4]. Recent high-fidelity single- [5] and two-qubit [6, 7] gate demonstrations show error probabilities of  $\sim 10^{-4}$  and  $\sim 10^{-3}$ , respectively, which likely can be improved further [8–12]. For this work, we assume that the inductive shunt in a fluxonium circuit constitutes a Josephson junction array (JJA) [13, 14] due to its relatively low loss, large inductance, and small capacitance. The internal modes of the fluxonium circuit identify a qubit mode, where the computational states reside, and several additional “parasitic” modes, from the charge islands in the junction array [15].

Typically, fluxonium qubit measurements are performed by dispersively coupling the circuit to a readout mode [5]. Dispersive readout, commonly used for its fast, single-shot capabilities, offers large signal-to-noise ratios and is expected to be quantum non demolition (QND) [16]. However, the fidelity and speed of this readout strategy has been limited by spurious transitions of the computational states to higher energy states [17–22], often called Measurement-Induced State Transitions (MIST). Unlike the weakly anharmonic transmon, a fluxonium circuit is highly nonlinear [3], which increases the likelihood of MIST effects [23]. Additionally, any spurious modes, such as the JJA modes mentioned previously, box modes from chip packaging, or slot line modes in the chip geome-

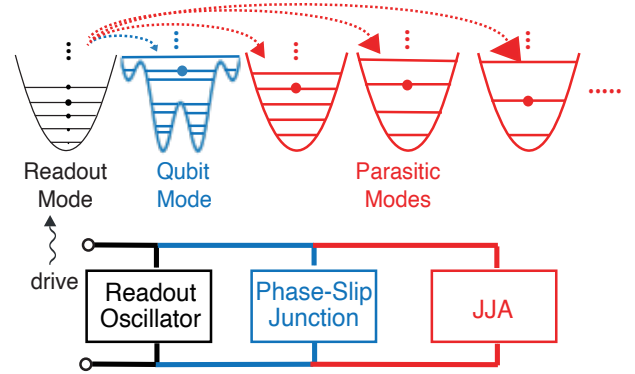


FIG. 1. Schematic of qubit state transitions driven by a readout resonator with parasitic modes from a Josephson junction array (JJA). The cartoon circuit diagram is paired with energy profiles, showing photon energy splitting into JJA parasitic modes (red), leaving enough for qubit excitation (blue).

try, may also play a role in MIST, as shown in Fig. 1. However, a detailed analysis of MIST in the presence of such spurious modes during dispersive readout of a superconducting qubit is still pending.

In this work, we analyze the state transitions during the dispersive readout of a fluxonium circuit, especially focusing on the effects that arise due to the parasitic modes of the JJA-fluxonium. Fig. 2 shows our measurement circuit for a heavy fluxonium circuit at the flux sweet spot ( $\varphi_{ext} = 0.5\Phi_0$ ), an experimentally-relevant choice for maximizing qubit coherence [2, 5, 24, 25]; however, parasitic effects in the case of several circuit modifications are also discussed. We study population in the first three eigenstates in the qubit mode, to include experiments with

\* Corresponding email: shraddha.singh@yale.edu

† Present address: Google Quantum AI, Santa Barbara, CA

a heavy fluxonium that use the first two levels ( $|0\rangle$ ) for computation and the second two levels ( $|2\rangle$ ) for measurement [5]. With our Hamiltonian derivations inspired from [26], we find that the coupling strength between the qubit mode and the parasitic modes can be  $\sim 100$  MHz, approximately ten-fold higher than the qubit-readout coupling strength. Treating the

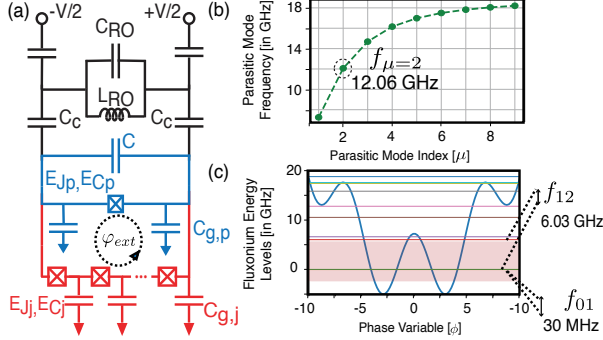


FIG. 2. (a) Fluxonium readout circuit. The color scheme uses Fig. 1 where readout oscillator (RO) is connected to a JJA fluxonium circuit. This circuit shows parasitic ground capacitances in JJA ( $C_{g,j}$ ) and next to phase-slip junction ( $C_{g,p}$ ), coupling capacitances ( $C_c$ ), linear RO with frequency ( $\omega_r/2\pi = 1/\sqrt{L_{RO}C_{RO}}$ ). The phase-slip junction capacitance is adjusted with the differential capacitance  $C$ .  $V$  denotes the drive strength. (b) Parasitic mode  $\omega_\mu$  frequencies. The closest even mode  $\mu = 2$  has the strongest coupling to the qubit (see Fig. 13). (c) Fluxonium mode  $\phi$  energy levels, with the highlighted area showing the first three levels essential for certain readout schemes [5].

$N$	$\varphi_{ext}$	$E_{J_p}$	$E_{C_p}$	$E_C$	$E_{C_j}$	$E_{J_j}$	$E_{C_{g,j}}$	$E_{C_{g,p}}$	$E_c$
122	$0.5\Phi_0$	7.30	0.74	1.34	0.74	60	194	1.94	19.40

TABLE I. Circuit parameters for Fig. 2(a). All energies are given in GHz. Here  $\Phi_0 = h/2e$  denotes the magnetic flux quantum. The capacitive energies  $E_{C'} = \frac{19.4}{C'(fF)}$  GHz are computed from the corresponding capacitances  $C'$ . See Table V in App. B for values of capacitances.

readout mode classically [20, 21], we perform a Floquet simulation of this system and identify predominant MIST effects, shown in Fig. 3. In particular, our simulation of the dispersive readout process identifies state transitions of the fluxonium mode under dispersive readout, which occur only in the presence of the coupling between the qubit mode and the parasitic mode. We term these phenomena parasitic-mode-assisted MIST (p-MIST). At particular readout resonator frequencies, we find that the onset of p-MIST can occur with only  $\sim 10$  photons in the readout resonator, well within the desired power for high signal-to-noise ratios in dispersive readout [27].

Our work identifies transition pathways not seen in previous Transmon-based MIST analyses, which occur because of the highly nonlinear nature of the fluxonium spectrum. To understand the Floquet simulation results, we identify the processes that cause these transitions in Table. III using energy-conservation processes which are supported by a perturbative estimation from Fermi's Golden rule calculations. The total number of MIST effects increase by 50% in

the presence of the parasitic mode with the strongest coupling to the qubit mode. Examples of some interesting MIST effects are as follows. A higher energy fluxonium state ( $|2\rangle$ ) may exchange population with a lower energy state ( $|0\rangle$ ), through excitation exchange with the readout resonator in the presence of a parasitic mode. In our simulations, we also observe that two higher fluxonium states are hybridized into an equal superposition state when the drive frequency is resonant with their transition frequency; such hybridization allows for increased p-MIST effects. We also observe transitions between parity conserving states which are impossible via a first-order process for  $\varphi_{ext} = 0.5\Phi_0$ .

We compute the rates of all p-MIST effects involving the  $|1\rangle$  state, which is involved in both measurement and computation, to justify that the observed MIST effects can be significant. The rates are computed the quasi-energy gap obtained via the Floquet simulations in Landau-Zener probability calculations. These calculations show that p-MIST effects with avoided crossings of the order of  $\sim 1$  MHz occur at significant probability. The avoided crossings of such strong transitions can be correctly predicted using first-order perturbative calculations. We provide information on the avoided crossing and first-order FG rates of each transition in App. C3. We also discuss the the Hamiltonian dynamics of the system in App. C3. Additionally, we show that the residual p-MIST population in the parasitic modes, which remains after a readout pulse, begets significant dephasing of the qubit mode. Since these parasitic modes are long-lived [13] and strongly coupled to the qubit mode, such residual population must be treated with care when designing the circuit. We numerically show that the dephasing error probability due to excited parasitic modes with finite internal quality factor is above the surface code error correction threshold. This effect indicates that, without proper care, the dephasing due to p-MIST could limit the performance of a fluxonium qubit architecture.

Finally, we generalize our results to several circuit modifications by analyzing the sensitivity of the parasitic mode-qubit coupling strength for different grounding configurations, readout frequencies, parasitic mode frequencies, qubit mode frequencies, ground capacitances and number of junctions in the array. First, we show that these effects are mediated strictly by the coupling between the qubit mode and the parasitic mode. We also explore lower readout frequencies and show that increased p-MIST effects can be introduced if the parasitic frequency is an integer multiple of the drive frequency in Fig. 9. We also simulated a  $\sim 300$  MHz circuit with larger parasitic mode frequencies, inspired by the experiment in Ref. [6]. We find that for comparable frequencies and coupling strengths this circuit has much lower number of MIST, and even in this case half the transitions are p-MIST. While our analysis does not demonstrate an exhaustive study over the entire parameter space, it shows that the parasitic modes of a junction array introduce additional constraints on circuit design of high-coherence fluxonium qubits.

Qubit Readout Parameters	$\omega_{01}/2\pi$	$\omega_{12}/2\pi$	$\tilde{E}_c^\phi$	$g_{\phi r}/2\pi$	$\chi_{\phi r}(01)/2\pi$	$\chi_{\phi r}(12)/2\pi$	$\omega_r/2\pi$	$\kappa_r/2\pi$
-	30 MHz	6.04 GHz	0.92 GHz	25.50 MHz	0.18 MHz	0.98 MHz	8.50 GHz	1 MHz
Parasitic-Mode Parameters	$\delta\omega_{01,\mu}/2\pi$	$\delta\omega_{12,\mu}/2\pi$	$g_{\phi\mu}/2\pi$	$g_{\mu r}/2\pi$	$\chi_{\phi\mu}(01)/2\pi$	$\chi_{\phi\mu}(12)/2\pi$	$\omega_\mu/2\pi$	$\bar{n}_\mu$
( $\mu = 2$ )	0.40 MHz	14 MHz	157 MHz	4.22 MHz	-1.10 MHz	5 MHz	12.06 GHz	$(T = 20\text{mK})$ $6.3e - 8$

TABLE II. Qubit readout and closest even mode parasitic mode ( $\mu = 2$ ) parameters. (Qubit Mode)  $\omega_{01}$ : fluxon/qubit frequency,  $\omega_{12}$ : plasma frequency,  $\tilde{E}_c^\phi$ : qubit charging energy,  $g_{\phi r}$ : qubit-readout coupling,  $\chi_{\phi r}(ij)$ : dispersive shift due to parasitic modes in the two-level  $ij$  system,  $\omega_r$ : readout mode frequency,  $\kappa_r$ : decay rate. These quantities are derived and computed analytically using derivations in [26], also detailed in App. A. (Parasitic Mode)  $\omega_\mu$ : mode frequency,  $\delta\omega_{01,\mu}$ : fluxon frequency correction,  $\delta\omega_{12,\mu}$ : plasmon frequency correction,  $g_{\phi\mu}$ : qubit-parasitic coupling,  $g_{\mu r}$ : parasitic-readout coupling,  $\chi_{\phi\mu}(ij)$ : dispersive shift due to parasitic modes in the two-level  $ij$  system, and  $\bar{n}_\mu$ : thermal population at 20 mK.

The article is structured as follows: Sec. II details the readout circuit and its strong parasitic coupling under a linear JJA approximation. Sec. III covers readout dynamics, including MIST effects and dephasing from parasitic modes. Sec. IV analyzes coupling trends between parasitic, qubit, and readout modes across various circuit modifications. Finally, in Sec. V we discuss future readout strategies not covered in this analysis.

## II. FLUXONIUM READOUT CIRCUIT

We consider a JJA-fluxonium circuit dispersively coupled to a readout mode as shown in Fig. 2. The parameters for circuit design used in our work, listed in Table I, are motivated by recent experiments [5, 7]. We focus on the fluxonium circuit at the “sweet spot” for maximal qubit coherence times. This choice also reduces the number of allowed transitions in the circuit, as transitions between parity-conserving states via first-order processes are forbidden in this case. Here, the qubit frequency ( $\omega_{01}/2\pi$ ) is  $\sim 30$  MHz and the plasmon frequency ( $\omega_{12}/2\pi$ ) is  $\sim 6$  GHz, in this “heavy” fluxonium regime (see Table II for a full list of readout parameters). The dispersive shift on the qubit computational states due to the readout resonator is not sufficiently strong for high signal-to-noise, at  $\chi_{01} \sim 0.2$  MHz; in practice, higher excited states of the fluxonium qubit mode may be populated for improved readout fidelity [5]. Thus, to capture effects from measurement schemes that use higher levels (1, 2), we consider the population in the lowest three states of the qubit mode.

Our work specifically investigates the role of the JJA, which comprises the inductive shunt of the fluxonium. The array comprises  $N + 1$  junctions and  $N$  ground capacitances due to the JJA ( $C_{g_n}$ ) [25]. We assume an ordered array with identical junctions and parasitic ground capacitances between these junctions ( $C_{g_1} = \dots = C_{g_{N-1}} = C_{g,j}$ ). Two additional ground capacitances near the phase-slip junctions may have different values, with  $C_{g_0} = C_{g_N} = C_{g,p} \neq C_{g,j}$ . The JJA fluxonium circuit has  $N$  internal degrees of freedom [15, 26]: one qubit mode ( $\phi$ ) and  $N - 1$  parasitic modes ( $\mu$ ), where  $\mu$  ranges between 1, ...,  $N - 1$ . These modes are coupled via the ground capacitances. In our notation, we label the readout mode as  $r$ . The qubit

charge and flux quadratures are denoted by  $\hat{N}_\phi$  and  $\hat{\phi}$  where  $[\hat{\phi}, \hat{N}_\phi] = \frac{i\hbar}{2}$ . We denote the photon loss and gain operators using  $\hat{a}_r, \hat{a}_\mu$  and  $\hat{a}_r^\dagger, \hat{a}_\mu^\dagger$ , respectively. We simplify the problem by treating all but the qubit mode as harmonic oscillators as assumed in previous works [15, 21, 26]. With this assumption, we derive the circuit Lagrangian and Hamiltonian (see App. A). In units of  $\hbar = 1$ , the Hamiltonian of an undriven fluxonium measurement circuit has the form

$$\hat{H} = \hat{H}_\phi + \hat{H}_\mu + \hat{H}_r + \hat{H}_{int}, \quad (1)$$

where the qubit Hamiltonian  $\hat{H}_\phi$  (with JJA inductive energy  $E_L = E_{J_j}/N$ ) is

$$\hat{H}_\phi/2\pi = 4\tilde{E}_c^\phi \hat{N}_\phi^2 + E_{J_p} \cos \hat{\phi} + E_L \hat{\phi}^2/2, \quad (2)$$

the junction array and readout Hamiltonians are  $\hat{H}_\mu = \sum_\mu \omega_\mu \hat{a}_\mu^\dagger \hat{a}_\mu$  and  $\hat{H}_r = \omega_r \hat{a}_r^\dagger \hat{a}_r$ , respectively. The qubit charging energy deviates from the target value of  $E_c^\phi = 1$  GHz due to parasitic capacitance. The coupling between the three modes is described by the interaction Hamiltonian

$$\begin{aligned} \hat{H}_{int} = & g_{\phi r} \frac{\hat{N}_\phi}{N_{\phi,ZPF}} (\hat{a}_r - \hat{a}_r^\dagger) \\ & - \sum_\mu g_{\phi\mu} \frac{\hat{N}_\phi}{N_{\phi,ZPF}} (\hat{a}_\mu - \hat{a}_\mu^\dagger) \\ & - \sum_\mu g_{\mu r} (\hat{a}_r - \hat{a}_r^\dagger) (\hat{a}_\mu - \hat{a}_\mu^\dagger). \end{aligned} \quad (3)$$

where the zero-point fluctuation value is  $N_{\phi,ZPF} = 1.4$ . All Hamiltonian variables in this Hamiltonian are given in Table. II.

Our coupling strengths follow the same relative behaviour as observed in Ref. [26], but with a different set of parameters as chosen here. We find that the lowest-frequency even parasitic mode  $\mu = 2$  has the strongest coupling to the qubit mode (see Fig. 13 in App. B); parasitic parameters are quoted in Table I. Ref. [26] shows that the symmetry of the parallel circuit in Fig. 2 prevents coupling between odd parasitic modes (including  $\mu = 1$ ) and other circuit modes. We extend this result to two additional circuits, with different ground circuit configurations, showing qualitatively consistent conclusions across all in App. A. The

circuits yield the same Hamiltonian when the differential capacitance  $C$  and coupling capacitance  $C_c$  are altered such that qubit frequency and qubit-readout coupling are same across all three circuits (see Table IV in App. A). With these observations, in the rest of this work, we will use the parallel circuit from Fig. 2 and Tables I, II in Eq. 1 with only consider a three modes, the qubit ( $\phi$ ), the strongest coupled parasitic mode ( $\mu = 2$ ) and the readout resonator ( $r$ ). For details on other parasitic modes and their circuit parameters, see Apps. B and A.

As reported in Table I, the qubit couples roughly six times more strongly to the parasitic mode at  $\mu = 2$  than it does to the readout  $r$ . (In fact, there are four parasitic modes with coupling strengths within a factor of 10 of  $g_{\phi r}$ ). This strong coupling indirectly couples the readout with the parasitic modes, through the qubit mode with strength  $g_{\mu r} \propto g_{\phi \mu}$ . As we highlight in the next section, such strong couplings can lead to measurement-induced state transitions assisted by parasitic modes, termed “p-MIST”.

### III. PARASITIC-MODE-ASSISTED MIST: P-MIST

In this section, we will analyze how the presence of a parasitic mode ( $\mu = 2$ ) affects the dynamics of a driven fluxonium circuit in a readout context. To simulate the linear drive on the readout resonator, we add a drive term  $V_d = i\xi(\hat{a}_r - \hat{a}_r^\dagger) \cos \omega_d t$  to the system Hamiltonian in Eq. 1. If we consider the fluxonium qubit mode, parasitic modes, and readout resonator, numerical analyses of several excitations in the circuit would require a prohibitively large Hilbert space. For example, the highly nonlinear nature of the fluxonium qubit spectrum results in a minimum Hilbert space dimension of at least  $\sim 20$  for an accuracy of XXX, while we expect to drive many photons in the readout cavity. To truncate our Hilbert space to feasible dimensions for numerical simulations, here we only include a single parasitic mode  $\mu = 2$  (as previously justified in Sec. II), and we replace the readout mode with a classical drive term [18, 20, 21] using the derivation in App. C. Under this semi-classical approximation, we the Hamiltonian of only two modes ( $\phi$  and  $\mu = 2$ )

$$\hat{H}_{s.c.}(\bar{n}_r) = \hat{H}_0 + \hat{V}_{s.c.}(\bar{n}_r) \quad (4)$$

which includes the parent Hamiltonian,

$$H_0 = \hat{H}_\phi + \hat{H}_\mu - \frac{g_{\phi\mu}}{N_{\phi,ZPF}} \hat{N}_\phi (\hat{a}_\mu - \hat{a}_\mu^\dagger) \quad (5)$$

and the modified drive term  $V_{s.c.}$ ,

$$\hat{V}_{s.c.}(\bar{n}_r) = \frac{\xi_{\phi r}(\bar{n}_r)}{N_{ZPF,\phi}} \hat{N}_\phi \cos \omega_d t + \xi_{\mu r}(\bar{n}_r) \hat{N}_\mu \cos \omega_d t, \quad (6)$$

where  $\xi_{\mu(\phi)r}(\bar{n}_r) = 2g_{\mu(\phi)r}\sqrt{\bar{n}_r}$ , and  $\bar{n}_r$  denotes average readout photons, respectively. We shall call the quantities  $\xi_{\phi r/\mu r}$  qubit and parasitic drive strengths, respectively.

Our primary task is to analyze p-MIST effects which introduce simultaneous transitions in the parasitic mode and the qubit mode. To identify the state transitions in the driven circuit, we first examine the eigenspace of  $H_0$ . Commonly, for the analysis of a fluxonium circuit, the basis  $|k\rangle_\phi \otimes |n\rangle_\mu$  is used, where the parasitic mode  $\mu$  is mostly ignored [23]. We label the hybridized eigenstates of  $H_0$  as  $|\tilde{k}, \tilde{n}\rangle$  to indicate the states with maximum overlap in the disjoint Hilbert space  $|k\rangle_\phi \otimes |n\rangle_\mu$ . This labeling will helps us better understand the effects of p-MIST on the qubit subspace.

Next, we perform a Floquet simulation of the driven circuit to identify the state transitions in the system. We simulate the system dynamics for a range of readout resonator frequencies,  $\omega_d$ , and ring up the various drive strengths  $\xi_{\mu/\phi}$  to emulate the addition of photons in the readout resonator. We find that the presence of the parasitic mode  $\mu = 2$  significantly increases the number of MIST effects in the system. We analyze the processes that cause these transitions and quantify their rates using perturbative approaches and Landau Zener probability calculations [28]. We also show that the residual population in the parasitic modes, after a readout pulse, can lead to significant dephasing of the resetted qubit mode, limiting the performance of the qubit for any future use.

#### A. Floquet Simulations

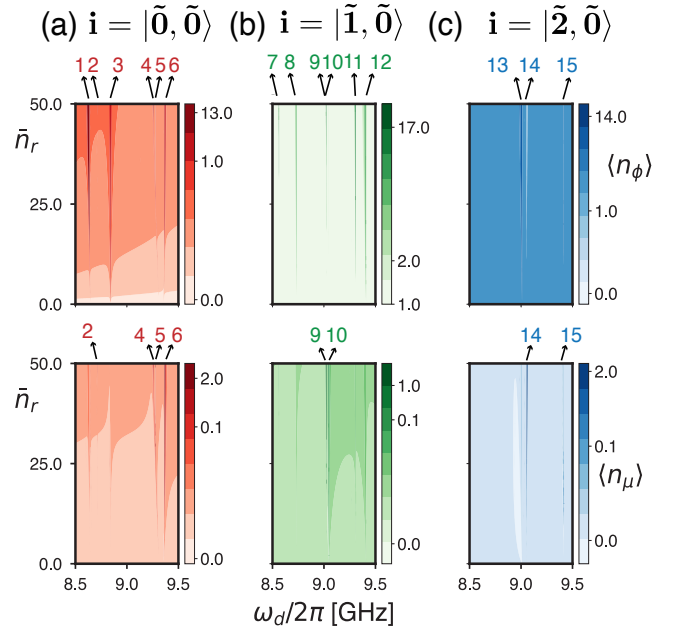


FIG. 3. p-MIST effects in Floquet Simulations. Columns show results for branch analysis starting in the dressed hybridized eigenstate  $i = |\tilde{k}, \tilde{0}\rangle$ , with maximum overlap to the un-hybridized states  $|k\rangle_\phi \otimes |0\rangle_{\mu=2}$ . (Top row) Average fluxonium excitation  $\langle n_\phi \rangle$ . (Bottom row) Average excitation  $\langle n_\mu \rangle$  of the first-even parasitic mode ( $\mu = 2$ ). The colorbar is in log scale for visual aid. Marked transitions are explicitly listed in Table III. See Figs. 17-19 of App. C 3 for quasienergies.



Our first numerical analysis uses Floquet simulation of the Hamiltonian  $H_{s.c.}$  (see Eqs. 4) while varying  $\bar{n}_r$  as the Floquet parameter, for various drive frequencies  $\omega_d$ . To reduce the numerical complexity, we only focus on transitions involving lowest 20 levels in the qubit subspace  $\phi$  and 3 levels in the harmonic oscillator mode  $\mu = 2$ . In App. C1 we discuss the truncation used to obtain our results. As indicated before, we will study transitions from states  $|i\rangle = |\tilde{\phi}, \tilde{\mu}\rangle$  where  $\phi = \{0, 1, 2\}$  and  $\mu = 0$ . With  $\omega_\mu = 12.06$  GHz, the analysis in this section will consider the regime of negative detuning where,  $\omega_{\mu=2} > \omega_d = \omega_r \gg \omega_q$ , and can be replicated for any other parasitic mode. We also analyze effects of an alternative circuit with  $\omega_{\mu=2}, \omega_\phi$  in Sec. IV

Inspired by [20, 21], we extract p-MIST effects by tracking a hybridized fluxonium eigenstate  $|i\rangle$  in a Floquet simulation while ringing up the drive strengths, a method known as *branch analysis*. Our drive ring-up emulates the addition of a single readout photon by incrementing  $\bar{n}_r$  for each tracking step at  $t = 0$ . The simulation begins in an eigenstate  $|i\rangle$  of the circuit Hamiltonian  $\hat{H}_0$ . This eigenstate is the same as the dressed eigenstate of  $H_{s.c.}$  at  $\bar{n}_r = 0$ ,  $|i\rangle_{\bar{n}_r=0}$ . Next, we compute the dressed eigenstates of the modified Hamiltonian  $\hat{H}_{s.c.}$  at  $\bar{n}_r = 1$ , corresponding to a single photon increase in the readout resonator,  $\{|m\rangle_{\bar{n}_r=1}\}$ . We then track the eigenstate  $|i\rangle_{\bar{n}_r=1}$  in this new eigenspace that has maximum overlap with  $|i\rangle_{\bar{n}_r=0}$ , identifying it as the new eigenstate associated with the branch of  $|i\rangle$ . This process is repeated with the increment  $\Delta\bar{n}_r = 1$ , such that at each tracking step  $t_k$ , a new state is chosen from the Floquet eigenspace of the modified Hamiltonian as, yielding the branch

$$|i_{\bar{n}_r=k}\rangle : \max_m |\langle i_{\bar{n}_r=k-1} | m_{\bar{n}_r=k} \rangle|^2. \quad (7)$$

Our method is different from Ref. [20, 21] in that we perform the branch analysis of the modified Hamiltonians  $H_{s.c.}(\bar{n}_r)$  at a fixed time  $t = 0$  while directly varying  $\bar{n}_r = 0$ . For each  $|m_{\bar{n}_r=i}\rangle$  tracked in the branch, we compute:

1. the average expectation values of  $\hat{n}_\phi = \sum_i i |i_t\rangle \langle i_t|$  where  $i_t$  are the bare fluxonium eigenstates,
2. the expectation value of  $\hat{n}_\mu = a_\mu^\dagger a_\mu$ , i.e., the number operator of the harmonic oscillator defined by the parasitic mode, and
3. the quasi-energy spectrum  $E_i \bmod \omega_d$ .

Fig. 3 illustrates our main result, showing p-MIST for initial states that have maximum overlap with states  $|0\rangle_\phi$ ,  $|1\rangle_\phi$  and  $|2\rangle_\phi$  in the fluxonium subspace and the ground state  $|0\rangle_{\mu=2}$  in the parasitic subspace. We focus on readout drive frequencies between 8.5 – 9.5 GHz [29] while other ranges of readout frequencies are also discussed in Sec. IV. The figure is plotted in log scale and any streak or sharp change in color represents a sudden and significant jump in the respective population, or MIST. The p-MIST effects correspond to simultaneous jumps in the population

of the modes  $\phi$  (Figs. 2a-2c, top row) and  $\mu = 2$  (Figs. 2a-2c, bottom row), as  $\bar{n}_r$  varies. At these points, an avoided crossing in quasi-energies confirms the hybridization of the two states involved in the population exchange (see Figs. 17-19 in App. C3). Additional resonances may occur at alternate drive frequencies not shown in Fig. 3. Table III lists significant transitions observed in our Floquet simulations, and associated processes which cause them, identified through a perturbative analysis (see App. C3) and energy conservation (shown later Fig. 8). We note that certain MIST effects, p-MIST or not, involve the unexpected transitions at the flux sweet spot [30] between parity-conserving states, due to virtual excitations via non-parity-conserving states.

The p-MIST effects occur only when qubit-parasitic mode coupling ( $g_{\phi\mu}$ ) is non-zero, covering roughly half the number of transitions listed in Table. III. This aspect is analyzed in Sec. IV. Such transitions will not be captured if parasitic modes are ignored in the Floquet simulations. An interesting instance is 15, where if the parasitic mode was absent the transition  $|17, 0\rangle \leftrightarrow |2, 0\rangle$  takes place which is a 3 readout photon process, however, in the presence of parasitic mode  $\mu = 2$  this process is broken down to be mediated by the hybridized states  $|\tilde{5}, \tilde{1}\rangle$  via two 1 readout and 2 readout processes. The number of p-MIST effects will increase when other parasitic modes, with coupling comparable to or greater than the qubit-readout coupling ( $\mu = 4, 6$ ), are included in the Floquet simulations. See Fig. 13 for absolute coupling strengths. Thus, ignoring parasitic modes can lead to wrong prediction of MIST free drive frequencies as well as sometimes may contribute wrong post-MIST state knowledge.

In transition 13, we observe downward transitions from a higher fluxonium level ( $|2\rangle_\phi$ ) to a lower fluxonium level ( $|0\rangle_\phi$ ), a process that would not be observed in the absence of parasitic modes, as it indicates emission of transition photons instead of absorption readout photons. This is possible because in the presence of parasitic mode, the state  $|\tilde{0}, \tilde{2}\rangle$  has a higher energy compared to  $|\tilde{2}, \tilde{0}\rangle$  such that absorbing two readout photons results in a p-MIST which is closest to a downward state transition in the disjoint fluxonium subspace.

In transitions 3 – 5 we observe Rabi Flopping between two states upon addition of a single photon, such that, the states hybridize into an equal superposition of the two states involved. For example, in transitions 4, 5, levels  $|3\rangle_\phi$  and  $|6\rangle_\phi$  converge to a population of  $\langle n_\phi \rangle = 4.5$  in the fluxonium subspace at  $\bar{n}_\mu \rightarrow 0$  (see Fig. 17 in App. C3). While this effect is not limited to p-MIST, we highlight the presence of these effects as an accelerator to p-MIST effects since for each transition frequency  $\omega_{ij}$  in the fluxonium subspace there are several possible transitions  $|\tilde{i}, \tilde{n}_\mu\rangle \rightarrow |\tilde{j}, \tilde{n}_\mu\rangle$ , for all  $\bar{n}_\mu$ . A result of this effect is that a parasitic process  $|\tilde{6}, \tilde{1}\rangle \leftrightarrow |\tilde{0}, \tilde{0}\rangle$  which is a 5 readout-photons process will now only require 2 readout photons, thus increasing the chances of an avoided crossing.

The MIST effects with no jumps in the qubit sub-

S.No.	MIST	Drive Frequency ( $\omega_d$ )	p-MIST	Process (see App. C3 and Fig. 8)
1.	$ \tilde{0}, \tilde{0}\rangle \xleftarrow{\bar{n}_r=13}  \tilde{13}, \tilde{0}\rangle$	8.64 GHz	×	(3r)
2.	$ \tilde{0}, \tilde{0}\rangle \xleftarrow{\bar{n}_r=48}  \tilde{4}, \tilde{2}\rangle^*$	8.71 GHz	✓	(2r)→(4r)
3.	$ \tilde{0}, \tilde{0}\rangle \xleftarrow{\bar{n}_r \rightarrow 0}  \tilde{8}, \tilde{0}\rangle$	8.84 GHz	×	(2r)
4.	$ \tilde{0}, \tilde{0}\rangle \xleftarrow{\bar{n}_r=26}  \tilde{6}, \tilde{1}\rangle^*$	9.25 GHz	✓	(2r)→(1r)
5.	$ \tilde{0}, \tilde{0}\rangle \xleftarrow{\bar{n}_r=48}  \tilde{6}, \tilde{1}\rangle^*$	9.28 GHz	✓	(2r)→(1r)
6.	$ \tilde{0}, \tilde{0}\rangle \xleftarrow{\bar{n}_r=12}  \tilde{3}, \tilde{1}\rangle$	9.36 GHz	✓	(2r)
7.	$ \tilde{1}, \tilde{0}\rangle \xleftarrow{\bar{n}_r=32}  \tilde{17}, \tilde{0}\rangle$	8.56 GHz	×	(4r)
8.	$ \tilde{1}, \tilde{0}\rangle \xleftarrow{\bar{n}_r=4}  \tilde{7}, \tilde{0}\rangle$	8.73 GHz	×	(2r)
9.	$ \tilde{1}, \tilde{0}\rangle \xleftarrow{\bar{n}_r=19}  \tilde{12}, \tilde{1}\rangle$	9.02 GHz	✓	(4r)
10.	$ \tilde{1}, \tilde{0}\rangle \xleftarrow{\bar{n}_r=13}  \tilde{2}, \tilde{1}\rangle$	9.05 GHz	✓	(2r)
11.	$ \tilde{1}, \tilde{0}\rangle \xleftarrow{\bar{n}_r=8}  \tilde{14}, \tilde{0}\rangle$	9.31 GHz	×	(3r)
12.	$ \tilde{1}, \tilde{0}\rangle \xleftarrow{\bar{n}_r=3}  \tilde{9}, \tilde{0}\rangle$	9.41 GHz	×	(2r)
13.	$ \tilde{2}, \tilde{0}\rangle \xleftarrow{\bar{n}_r=2}  \tilde{12}, \tilde{0}\rangle$	9.00 GHz	×	(2r)
14.	$ \tilde{2}, \tilde{0}\rangle \xleftarrow{\bar{n}_r=37}  \tilde{0}, \tilde{2}\rangle$	9.06 GHz	✓	(2r)
15.	$ \tilde{2}, \tilde{0}\rangle \xleftarrow{\bar{n}_r=13}  \tilde{5}, \tilde{1}\rangle^*$	9.41 GHz	✓	(1r)→(2r)

TABLE III. Measurement-induced-state-transitions observed in Fig. 3. Column 1 lists the MIST effects that start at the lowest average readout photon number  $\bar{n}_r$ . In some cases, the label  $\bar{n}_r \rightarrow 0$  indicates that the drive frequency is exactly resonant with the transition frequency. An ‘\*’-marked state indicates hybridization at lower  $\bar{n}_r$  due to preceding transitions<sup>a</sup>. Column 2 represents the drive frequency  $\omega_d$  at which these transitions occur. Column 3 indicates if the process cannot occur without the parasitic mode, denoted as p-MIST. Column 4 indicates the number of readout photons ( $\#r$ ) involved in the energy-conserving process which is responsible for these transitions. We give comparison of Fermi’s golden rule rates and quasienergies for these processes in App. C3.

<sup>a</sup>  $|\tilde{4}, \tilde{2}\rangle^* : |\tilde{4}, \tilde{2}\rangle \xleftarrow{\bar{n}_r=5} |\tilde{14}, \tilde{2}\rangle$  at  $\omega_d = 8.71$  GHz  
 $|\tilde{6}, \tilde{1}\rangle^* : |\tilde{6}, \tilde{1}\rangle \xleftarrow{\bar{n}_r \rightarrow 0} |\tilde{3}, \tilde{1}\rangle$  at  $\omega_d = 9.25, 9.28$  GHz  
 $|\tilde{5}, \tilde{1}\rangle^* : |\tilde{5}, \tilde{1}\rangle \xleftarrow{\bar{n}_r=11} |\tilde{17}, \tilde{0}\rangle$  at  $\omega_d = 9.41$  GHz

space, also categorized as p-MIST, will only affect the parasitic modes during readout. However, after the qubit is reset post measurement, such an excited parasitic mode can severely dephase the resetted qubit. Our findings reveal that for our specific circuit choice JJA parasitic modes significantly many p-MIST effects are observed in the target readout range. Having identified key transitions that cause these effects we will now calculate how detrimental these processes can be towards qubit readout fidelity and coherence. To this end, we will next study some specific transitions in detail involving the state  $|\tilde{1}, \tilde{0}\rangle$  used for both computation as well as readout. We will analyze the probability of populating the parasitic modes in these transitions and its outstanding effect on the qubit coherence, post reset.

## B. Transition Probability

In this section, we estimate the quasienergies and rates of exemplary p-MIST transitions, using the Landau-Zener formalism, respectively. In both the Floquet simulations and Landau-Zener approximations, the spectral gap of an associated transition is a critical figure-of-merit in determining the diabatic energy exchange probability. Here, the avoided crossing of p-MIST transitions 9, 10 from Table III involving  $|\tilde{1}, \tilde{0}\rangle$ , the state involved in computation as well as readout [5], is shown in Fig. 4. The simultaneous exchange of population in the qubit mode  $\phi$ , shown

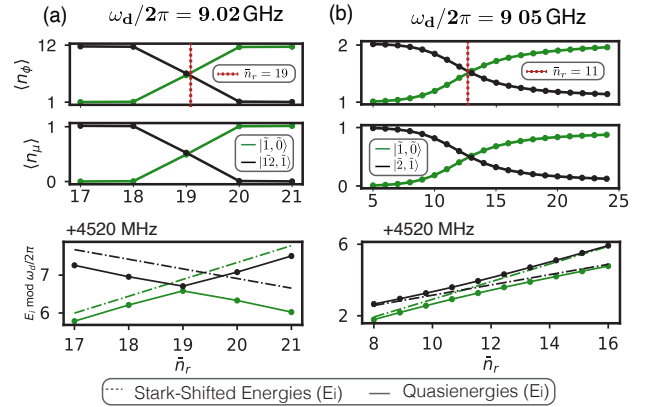


FIG. 4. Examples of p-MIST using transitions 9 (a) and 10 (b) from Table III involving the  $|\tilde{1}, \tilde{0}\rangle$  state. (Top row) Qubit mode average occupation  $\langle n_\phi \rangle$ . (Middle) Parasitic mode average occupation  $\langle n_\mu \rangle$  (Bottom) Stark-shifted eigen-energies from first-order perturbative calculations (dashed), and quasi-energies (solid) from Floquet simulations. The data points are connected by lines for visual aid. Plots are extracted from numerical data used in Fig. 3.

in Fig. 4(a), and the parasitic mode  $\mu = 2$ , shown in Fig. 4(b), confirms that the transitions are indeed p-MIST.

Here, Fig. 4(c) shows the avoided crossing at the transition point. For small drive amplitudes compared to the gaps in the spectrum, a simple estimate of the eigenenergies using perturbation theory is possible (see App. C2). The dashed lines in Fig. 4(c)

shows the eigenenergies calculated in App. C 2 by estimating the Stark shift from the readout drive onto each state. Comparing our Fermi's Golden rule estimates in App. C 3 to the numerically obtained energy gaps in the quasi-energies (solid lines), we find agreement within XXX. The transition shown in (a) is much stronger transition with  $\Delta_{ac} = .66$  KHz compared to (b) where  $\Delta_{ac} = 0.12$  KHz. The remaining disagreement between the quasi-energies and the estimated eigenenergies suggests that higher-order or non-perturbative corrections become relevant for transitions slower than  $\Delta_{ac} = XX$ . Notably, both the transitions shown in Fig. 4 occur at low average number of readout photons of  $\bar{n}_r = 12, 19$ , well within the power typically needed for high signal-to-noise dispersive readout of superconducting qubits [27].

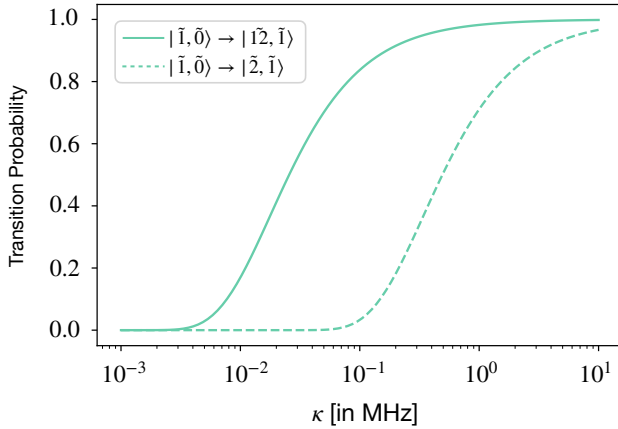


FIG. 5. Landau-Zener probability against the parameter  $\kappa$  which determines the change in drive strength  $\xi_{\mu/\phi} = 2g_{\mu/\phi}\sqrt{\bar{n}_r(t)}$  where  $n_r(t)$  follows Eq. 8. [SS: Yet to add unitary evolution curves]

Now, we will use these numerically-computed gaps in the quasi-energies to evaluate the Landau-Zener (LZ) probabilities, using the method described in Ref. [28]. For this analysis, we assume a time dependence of the average readout photon number of

$$\bar{n}_r(t) : \bar{n}_r(1 - e^{-\kappa_r t/2})^2, \quad (8)$$

which includes a ring-up time of  $1/\kappa$ , according to the readout resonator bandwidth [19–21]. Note that the time interval  $\Delta t$  is computed using  $\Delta\bar{n}_r = 1$ , thus replicating our previous model used for Floquet simulations with  $\bar{n}_r = 50$ . Varying  $\kappa$  changes the probability of transitions, plotted in Fig. 5 (for details see App. C 4). As expected, transition (a)  $|\tilde{1}, \tilde{0}\rangle \leftrightarrow |\tilde{2}, \tilde{1}\rangle$  is more probable than transition (b)  $|\tilde{1}, \tilde{0}\rangle \leftrightarrow |\tilde{12}, \tilde{1}\rangle$  as suggested by the comparison of their quasi-energy gap at the avoided crossing. This analysis shows that at  $\kappa/2\pi < 1$  MHz probability of transition (a) is significantly high. This value of decay rate is comparable to readout resonator  $\kappa_r$  (see Table II).

We compare these LZ transition probabilities to the overlap of the initial state evolved under the unitary  $U = e^{i\hat{H}_{s.c.}t}$  with the Floquet branch state at  $t_f = \frac{10}{\kappa_r}$ :  $|\langle m_{\bar{n}_r=n_f} | U(t_f) | i \rangle|^2$ . Unlike Ref. [21] we do not find perfect agreement in these two cases due to Landau-Zener-Stuckelberg transitions..? This indicates that

the two-state physics captured by Landau-Zener transitions may not be correct to study strengths of fluxonium transitions.

We have confirmed that an observed p-MIST can have significant probability during a fluxonium qubit readout. While this effect will directly affect the readout performance for our chosen set of readout parameters, we will now analyze its impact of the qubit coherence.

### C. Qubit Dephasing post-Readout

Here, we consider implications of p-MIST *after* the readout pulse is executed, in the context of a larger quantum circuit where the fluxonium mode is used as a qubit. In general, the parasitic modes are long-lived, with internal quality factors of  $\sim 10^4$ [13, 31]. Spurious excited state population of the parasitic mode introduced by p-MIST during readout can introduce correlated dephasing of the qubit, through the large dispersive interaction  $\chi_{\mu\phi}/2\pi \sim 1$  MHz (see Table I). If the parasitic mode is excited, the qubit accumulates a phase at a constant rate  $\chi_{\mu\phi}\bar{n}_\mu$ , in the absence of any decay i.e. infinite internal quality factor  $Q_\mu$ . This error can be measured and corrected for, given the knowledge of  $\bar{n}_\mu$ . However, for a finite  $Q_\mu$ , the parasitic mode decays at a rate  $\kappa_\mu = Q_\mu/\omega_\mu$ . In this scenario, the qubit dephasing is not deterministic but a Poissonian process which relies on the random decay of the parasitic mode. We have confirmed that dephasing due to the detuned drive and thermal effects is negligible (see App. C 5). Now, we will analyze this effect due to p-MIST induced excitation in the parasitic parasitic modes.

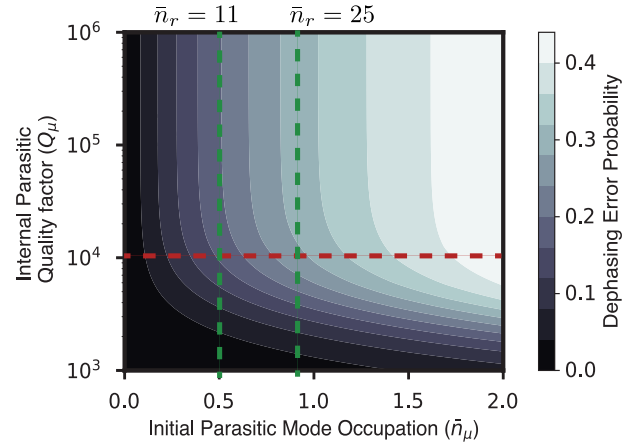


FIG. 6. Dephasing error probability due to random decay of an excited parasitic mode after p-MIST at finite  $Q_\mu$ . The horizontal red line shows the quality factor quoted in [13]. The green lines show the dephasing error probability for transition 10 (see Figs. 5, 4(b)) at different average readout photons.

Post the readout pulse in transition (b) for  $\kappa = 1$  MHz, we reset the fluxonium subspace to the qubit state  $|+\rangle = \frac{|0\rangle_\phi + |1\rangle_\phi}{\sqrt{2}}$ . The parasitic mode, however, remains in the excited state  $|1\rangle_{\mu=2}$  with some probability. To emulate the effect of this transition, we per-

formed a master equation simulation of a toy model where a disjoint qubit-cavity state  $|+, \bar{n}_\mu\rangle$  is evolved under the Hamiltonian  $H = \chi_{\phi\mu} \hat{a}_\mu^\dagger \hat{a}_\mu \sigma_z$ . During this evolution, the cavity (here, the parasitic mode) suffers dissipation under the decay operator  $\sqrt{\kappa_\mu} \hat{a}_\mu$ . We plot in Fig. 6 the infidelity of the qubit state with the  $|+\rangle$  state, after the parasitic mode reaches a steady state at  $T_f = 10/\kappa_\mu$ , for various  $Q_\mu$  and  $\bar{n}_\mu$ . Specifically, we find that for internal quality factors of the parasitic mode  $Q_\mu$  of  $10^4$ ,  $\langle n_\mu \rangle = 1$  population in the parasitic mode is needed to introduce a dephasing error probability,  $\sim 0.2$ , which is already past the threshold of surface code decoders [32]. Given that the population of the parasitic modes is about  $\bar{n}_\mu \sim 1$  at a readout power of  $\sim 10$  photons, we expect that qubit coherence can be limited by p-MIST in circuit designs which do not anticipate them.

We have provided quantitative evidence, with the help of various methods used in these analyses, that p-MIST effects can limit the performance of a fluxonium qubit architecture, without careful consideration of the parasitic modes during circuit design. In the next section, we will analyze the range of various mode frequencies responsible for these effects.

#### IV. EFFECTS OF CIRCUIT MODIFICATIONS ON P-MIST

The p-MIST effects shown in the previous section can be mitigated in various ways, by adjusting the qubit frequency, readout resonator frequency, and parasitic mode frequencies, as well as reducing parasitic mode and qubit coupling strengths. In this section, we explore the impact of each of these components individually. All equations analyzed in this section were derived in Ref. [26] for the circuit in Fig. 2, and we have extended these results to circuits with different grounding configurations in App. A.

##### A. Coupling Strengths

The strong coupling between the qubit and the parasitic mode is primarily responsible for MIST effects. Here, we show evidence of this, via Floquet simulations where various coupling constants are changed to zero to analyze their significance. Fig. 7 compares Floquet plots for the initial state  $|\tilde{1}, \tilde{0}\rangle$  under different coupling conditions. We can see from Fig. 7(b) that  $g_{\phi r}$  alone does not cause significant transitions or p-MIST effects without  $g_{\phi\mu}$ , as evident from the absence of transitions 9, 10 and no parasitic mode excitations in the bottom panel. The parasitic mode population in the absence of this coupling is restricted to  $\bar{n}_\mu = 10^{-4}$ . Turning both parasitic couplings (not shown here) off completely removes any population from the parasitic mode. For full Floquet landscape with quasi-energy see App. B2. Therefore, reducing the coupling strength  $g_{\phi\mu}$  is a potential path to mitigating MIST effects.

Here, we analyze the dependence of these coupling strengths on circuit and readout parameters. As

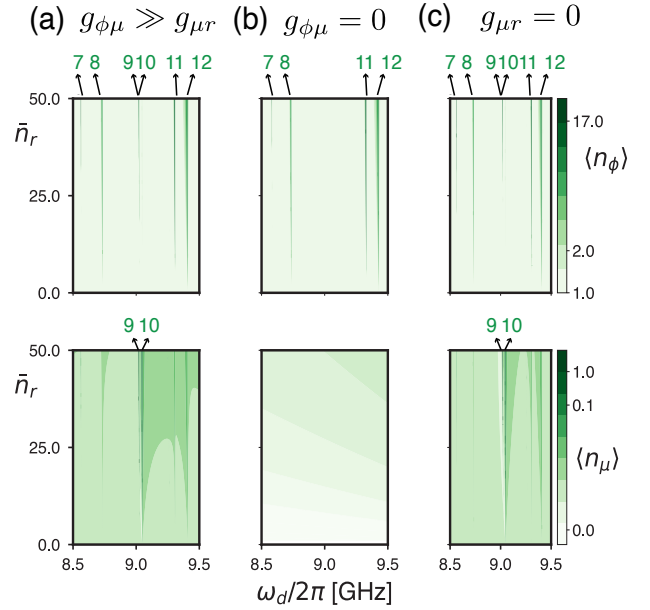


FIG. 7. Floquet Simulations for the Circuit parameters in Table I due to the various coupling terms. The marked transitions show the MIST effects observed in Fig. 3. (a) Same as Fig. 3(b). (b) Zero parasitic mode coupling to the qubit (c) Zero parasitic mode coupling to the readout.

derived in App. B and given in [26], the coupling strength  $g_{\phi\mu}$  is

$$g_{\phi\mu} = \sqrt{\frac{2}{N}} \frac{\tilde{E}_c^\phi \tilde{E}_{c,\mu}^e c_\mu}{E_{g_j} s_\mu^2} \cdot N_{\phi/ZPF} \cdot N_{\mu/ZPF} \quad (9)$$

where  $c_\mu = \cos \frac{\pi\mu}{2(N-1)}$ ,  $\tilde{E}_c^\phi, \tilde{E}_{c,\mu}^e$  are the qubit and parasitic mode charging energies, respectively, and  $N_{\phi/\mu,ZPF}$  are the zero-point fluctuation values for the qubit and parasitic modes. Expressions for  $\tilde{E}_{c,\mu}^e$  can be found in Eq. 13,  $\tilde{E}_c^\phi, N_{\phi/\mu,ZPF}$  can be found in App. B while all the other parameters are given in Table I.

By observation, suppressing the parasitic capacitance to ground near the junction array suppresses the qubit-parasitic coupling  $g_{\phi\mu}$ . However, this is constrained by practical limits of around 0.1 fF per junction due to the gap to the ground plane. For the parasitic modes with strongest coupling to the qubit  $\mu \ll N$ , the large  $N$  limit with  $c_\mu \approx 1$  yields

$$\tilde{E}_{c,\mu}^e \approx E_{g_j} s_\mu^2, \quad \tilde{E}_c^\phi \propto \frac{1}{N^2} \implies g_{\phi\mu} \propto \frac{1}{N^{5/2}}. \quad (10)$$

These dependencies are plotted in Fig. 14 of App. B. The trend with respect to  $N$  is not so straightforward. Note that changing  $N$  changes the target inductance of the qubit. Keeping the same inductance as  $N$  changes requires one to increase  $E_{J_j}$  by the same factor as  $N$ . To keep the  $E_{J_j}/E_{C_j}$  ratio the same this leads to an increase in  $E_{C_j}$ , thus extending our argument for large  $N$  even further. Both these tasks (increasing  $N$ , decreased  $C_{g,j}$ ) are hard at hand.



## B. Mode Frequencies

We can estimate the resonance conditions for a p-MIST effect by identifying energy-conserving processes, where  $m$  photons are converted into a transition  $\tilde{\Delta}_{if,n}$  in the hybridized eigenspace of the fluxonium and parasitic mode  $\mu = 2$ . Here,  $\tilde{\Delta}_{if,n}$  is the transition energy between levels  $|\tilde{i}, \tilde{p}\rangle$  and  $|\tilde{f}, \tilde{q}\rangle$  such that  $|p - q| = n$ . In the disjoint Hilbert space, this equation can also be interpreted as a process where  $m$  readout photons convert into  $n$  parasitic mode photons and a fluxonium excitation  $|i\rangle_\phi \leftrightarrow |f\rangle_\phi$  ( $\Delta_{if} = |E_f - E_i|$ ). To guide intuition for understanding the spectrum of resonance conditions, we plot such energy-conserving processes in Fig. 8, for the lowest-order case of  $\mu = 2$ , that satisfy

$$|m\omega_r - \tilde{\Delta}_{if,n}| \approx |m\omega_r - (n\omega_\mu + \Delta_{if})| \leq 25 \text{ MHz}, \quad (11)$$

where a buffer of 25 MHz is allowed to accommodate for Stark shift (see App. C2).

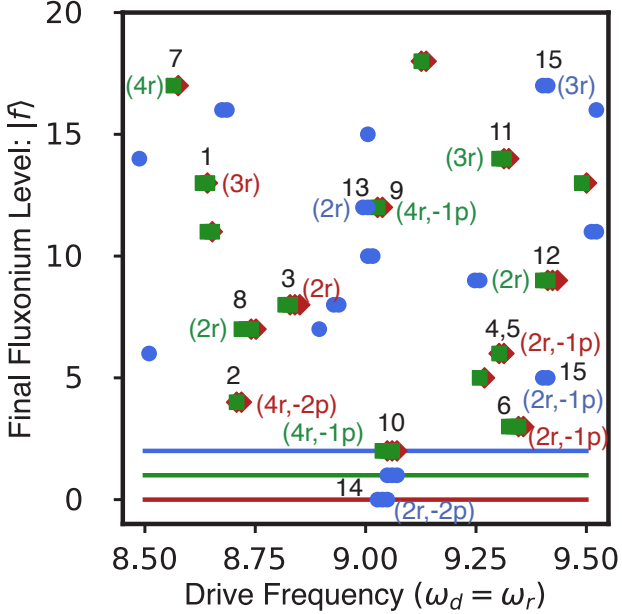


FIG. 8. Energy conserving processes  $|\tilde{i}, \tilde{0}\rangle \leftrightarrow |\tilde{f}, \tilde{n}_\mu\rangle$  for Eq. 11 for  $m \leq 4, n \leq 2, j \leq 20$  and  $i = 0$  (red),  $i = 1$  (green),  $i = 2$  (blue). The horizontal lines indicate the initial state for each color for visual aid. Labels in black correspond to transition # listed in Table III. Colored labels  $(m, -n)$  values of show the number of readout photons ( $m$ ) and the number of parasitic mode ( $\mu = 2$ ) photons ( $n$ ) involved in the transition.

The energy profile profile in Fig. 8 shows us the regions where up to four-photon processes will be prominent when starting in one of the four lowest fluxonium levels involved in the readout. Note that there are downward transitions from  $|2\rangle_\phi$  to  $|1\rangle_\phi, |0\rangle_\phi$  in the fluxonium subspace, in the presence of parasitic modes, one of which was captured in transition 15 of Table I. To emphasize the correctness of these predictions we mark all the transitions captured in the Floquet simulations (see Sec. III) in Fig. 8). The labels correspond to the disjoint subspaces for clarification

but the energy conservation uses the eigen-energies of the hybridized eigenstates of  $H_0$  in Eq. 4. A positive  $m, n$  denotes emission while a negative denotes absorption. For example, transition 2 emits 4 readout photons which is converted into 2 parasitic mode photons absorbed by the mode  $\mu = 2$  and the transition  $|0\rangle_\phi \leftrightarrow |4\rangle_\phi$  in the fluxonium subspace. This equation gives us the following intuition which we verify for different ranges of the various mode frequencies. A large gap between  $\omega_d$  and  $\omega_\mu$  would require a large  $m$  to trigger a p-MIST effect.

*a. Drive Frequency:* If  $\omega_d \gg \omega_{\mu=N-1}$ , the most fatal case would be excitation of a low-frequency parasitic mode to large  $n$  leaving just enough energy to produce excitation  $f$  in the Fluxonium subspace of significant charge matrix elements (see Fig. 12). However such large excitations could be less probabilistic. A proper investigation of this case requires a large Hilbert space and is beyond the scope of this work. A low frequency readout, on the other hand, would incur a large  $m$  and can have similar impact. We give the Floquet figure corresponding to a low frequency readout in Fig. 9 which looks severely more populated compared to Fig. 3. It is important to compare the rates of such transitions, however, the increase can be explained around 6 GHz. The rear end of this frequency range is the same as the plasmon energy and half the parasitic mode  $\mu = 2$  frequency. This logic already indicates that 5.5 – 6 GHz would be a bad range of frequencies for the current choice of parameters. However, for the purpose of readout, a lower  $\omega_d$  is not favorable due to thermal effects, and hence not analyzed in this work.

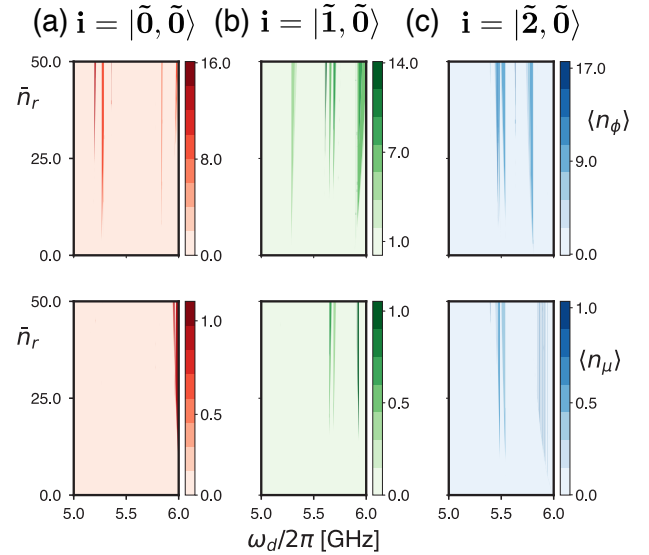


FIG. 9. Floquet simulations at lower readout frequencies for circuit parameters quoted in Table I. for starting the branch analysis in state  $i$ . The figures as before are plotted in log scale for visual aid.

*b. Parasitic Mode Frequency:* Another approach towards mitigating p-MIST effects is to adjust  $\omega_\mu$  so that  $\omega_r \ll \omega_\mu$  for  $\mu = 2$ , potentially improving the circuit. This is feasible with granular-aluminum (GrAl) inductive shunts, though they are lossy [27].

Recent efforts are being applied towards improving GrAI shunts.

For the JJA parameters, to provide some quantitative arguments in this direction we discuss the dependency of  $\omega_\mu$  for even parasitic modes ( $e$ ) on various circuit variables.

$$\frac{\omega_\mu^e}{2\pi} = \sqrt{8E_{c,\mu}^e E_{J_j}}, \quad \text{where} \quad (12)$$

$$E_{c,\mu}^e = \left[ \frac{1}{E_{C_j}} + \frac{1}{4E_{g_j}s_\mu^2} \right]^{-1}. \quad (13)$$

Here,  $s_\mu = \sin(\frac{\pi\mu}{2(N-1)})$ . Here,  $E_{c,\mu}^e$  is the charging energy of an even parasitic mode. All other variables used are defined in Table I. For parasitic modes with strong coupling,  $\mu \ll N$ , for large  $N$ , the charging energy is  $E_{c,\mu}^e \approx 4E_{g,j}s_\mu^2$ , which is inversely proportional to  $N^2$  and directly proportional to  $E_{g_j}$ . Again, a smaller parasitic ground capacitance  $C_{g_j}$  increases the parasitic mode charging energy, and thus desirably increasing its frequency. However, in contrast with the case of coupling strength  $g_{\phi\mu}$ , a larger  $N$  leads to lower frequencies for these modes, which is unfavorable. Fig. 14 in App. B shows the dependence of charging energy of parasitic modes as well as qubit modes with respect to parasitic ground capacitance. As stated before, the ground capacitance  $C_{g,j}$  is fixed while the impact of increasing  $N$  would require consideration of nonlinear corrections as well as fixed inductance, thus, making these changes difficult.

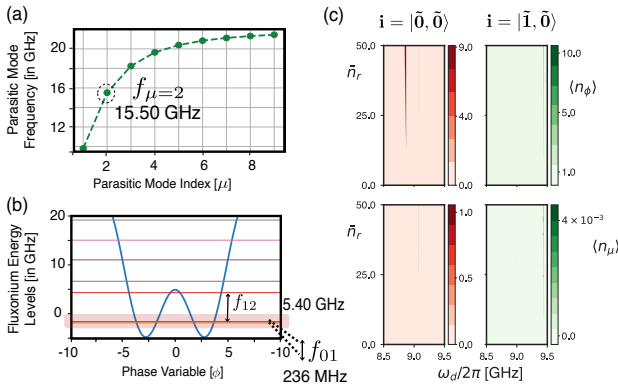


FIG. 10. MIST with alternate fluxonium circuit. (a) Fluxonium energy spectrum (b) Parasitic mode frequencies (c) Floquet simulations for the branch analysis of the computational states [33]. Circuit parameters for this circuit are given in App. D.

In the previous sections we focused on  $\sim 30$  MHz fluxonium frequency. To extend our results to other experiments, we consider another circuit inspired by parameters in [6] and show p-MIST effects in a 236 MHz fluxonium. The parasitic mode frequency of the  $\mu = 2$  mode is  $\omega_{\mu=2} = 15.51$  GHz. The coupling strengths are as follows,  $g_{\phi r} = 37$  MHz,  $g_{\phi\mu} = 216$  MHz,  $g_{\mu r} = 6$  MHz. The plasmon frequency is  $\omega_{12} = 5.40$  GHz. For these parameters, even though the coupling strengths are on par with Table I, since the parasitic mode frequency of the even mode  $\mu = 2$  is larger by  $\sim 4$  GHz, we expect fewer transitions. This has been verified in the Fig. 10 where only one

out of the three transitions is a p-MIST effect. Importantly, here we only plot results for  $|\tilde{0}, \tilde{0}\rangle$  and  $|\tilde{1}, \tilde{0}\rangle$  because given Ref. [6] uses only the first two levels for readout as well as computation. The detailed circuit parameters are given in App. D. The truncation for the simulation of this alternate circuit is discussed is shown in App. D.

Fig. 10 shows that the ratio of MIST and p-MIST effects is lower for this alternate circuit. We believe that the increased distance between the readout frequencies considered and the parasitic mode frequency owes to this feature. However, a detailed understanding of this Floquet profile is necessary to make proper claims in relation to severely reduced MIST effects, and is left as future direction.

## V. CONCLUSION AND FURTHER WORK

In this work, we have analyzed the impact of parasitic modes on the readout of a fluxonium qubit. This work shows that transitions in a fluxonium circuit triggered by a parasitic mode of the JJA, which we call p-MIST effects, can occur with considerable rates from coupling of the parasitic modes with the readout and qubit modes. The parallel circuit considered in this work utilizes a specific symmetry which removes the coupling between the lowest frequency mode and the qubit. We show that this symmetry is preserved if the readout resonator is coupling to a floating or grounded fluxonium at a single point. Our analysis considers fluxonium at the sweet spot which introduces additional symmetries forbidding transitions between parity-conserving states via first-order transitions. Despite these various symmetries and our modest assumption of no self-nonlinearity in the JJA or the readout, our results show that a strong coupling of parasitic modes to the qubit mode still triggers p-MIST at low average readout photons. Not only do p-MISTs lower the onset of MIST effects to  $\sim 10$  readout photons but also significantly dephase the qubit, both of which directly limit the readout fidelity [34].

We analyze the trend in p-MIST for various drive frequencies, parasitic mode frequencies, coupling constants, and circuits with two different qubit frequencies equal to  $\sim 30$  and  $\sim 300$  MHz. While our work does not constitute a thorough analysis of the entire parameter space by any means, it highlights the significant impact of parasitic modes in a driven fluxonium circuit. The assumptions we make are crucial to are MIST analysis. Increasing  $N$  can reduce the nonlinearity of the parasitic modes, with insights provided in Sec. IV. We also neglect the self-nonlinearity of the readout mode which has been a common practice in recent MIST-related analysis [17, 20, 21]. While the effects of nonlinearity in parasitic and readout modes can have significant impact on the readout fidelity, Floquet simulations including self-nonlinearity of these modes is beyond the scope of our work. Analysis of a disordered array could be an interesting extension of our work as it may lead to lower coupling between the qubit and parasitic modes. We analyze state transitions in a driven fluxonium circuit using

numerical methods under the following assumptions.

To advance practical implementation and reduce fluxonium MIST in the dispersive readout, we suggest adding noise to the Floquet framework [35] and linking our results to readout fidelity values using input-output theory. Future work should also incorporate the intrinsic nonlinearity of both the junction array modes and the readout mode. Mitigating parasitic mode excitations could involve varying junction energies along the array to localize collective modes, thereby altering the parasitic mode spectrum and reducing excitation probability. Alternative readout schemes like longitudinal readout or cloaking could also be explored [36–38]. Given the strong coupling between parasitic modes and fluxonium, these modes could potentially enhance fluxonium qubit readout. We propose using a feedline with a Purcell filter to tailor the spectrum and protect the qubit, reducing capacitive loading constraints.

Our results present a first analysis toward understanding the role of parasitic modes in the readout dynamics of a fluxonium circuit. Although the circuit parameters used in this work are closest to a fluxonium circuit, these results can be generalized to other high-anharmonic superconducting circuits with similar mode frequencies.

## VI. ACKNOWLEDGMENTS

We thank Akshay Koottandavida, Daniel K Weiss, Connor Hann, Kyungjoo Noh, and Simon Leiu for fruitful discussions. We are grateful to Simone Severini, Bill Vass, Oskar Painter, Fernando Brandão, Eric Chisholm, and AWS for supporting the quantum computing program.

### Appendix A: Single-Point Connections

The fluxonium readout circuit shown can have several modifications and each can affect various parameters associated with the efficiency of a fluxonium readout circuit as we proceed to show in this work. Here, in Fig. 14 we present two modifications to the parallel circuit shown in Fig. 2 with different grounding options for the fluxonium circuit. We will refer to these three circuit choices as  $H_1$  : (Parallel circuit, see circuit in Fig. 2),  $H_2$  : (Floating fluxonium, see left circuit in Fig. 14),  $H_3$  : (Grounded fluxonium, see right circuit in Fig. 14). Note that each parameter in Table. IV is significantly different for the three circuits. We adjust the coupling capacitance  $C_c$  and the total capacitance of the phase slip junction  $E_{C_p}$  (by modifying  $C'$ ) to achieve the same qubit frequency  $\omega_{01}$ , plasmon frequency  $\omega_{23}$ , qubit-readout coupling constant  $g_{\phi\mu}$  and qubit-readout dispersive shift  $\chi_{\phi r}$  for the three circuits as given in Table I. These modifications yield for circuit (b)  $E_{C_p} = 0.83$  GHz,  $E_{C_c} = 3.82$  GHz (c)  $E_{C_p} = 0.80$  GHz,  $E_{C_c} = 4.70$  GHz. Table. IV gives values of the various circuit parameters across the three circuits computed analytically using the expressions given in App. B. We note that upon ad-

Fluxonium Parameters ( $\mu = 2$ )	$H_1$ Parallel Circuit	$H_2$ Floating Fluxonium	$H_3$ Grounded Circuit
$g_{\phi\mu}$	157 GHz	161 GHz	158 GHz
$g_{\mu r}$	4.223 MHz	3.971 MHz	3.128 MHz
$\chi_{\phi,\mu}$	-1.1 MHz	-1.3 MHz	-1.1 MHz
$\delta\omega_{01,\mu}$	0.4 MHz	0.45 MHz	0.41 MHz

TABLE IV. Fluxonium parameters with the lowest frequency parasitic mode with non-zero coupling to the qubit and readout  $\mu = 2$ . Here we quote the frequency of the fluxon transition between the lowest two levels ( $\omega_{01}$ ) and the plasmon transition between the first and second levels ( $\omega_{12}$ ). For the dispersive Hamiltonian obtained for each circuit in Fig. 11(a-c), we quote the dispersive shift due to readout as  $\chi_r$ . The values in this table have been experimentally verified for  $H_1$ . The frequency of this mode is  $f_\mu = 12.063$  GHz. We give the coupling strengths between the qubit-readout  $g_{\phi\mu}$ , readout-parasitic  $g_{\phi r}$ , parasitic-qubit  $g_{\mu r}$  modes. We also give the Stark shift  $\chi_{\phi\mu}$  and frequency correction  $\delta\omega_{01,\mu}$  on the two-level system realized by this fluxonium circuit in the dispersive regime. Here the values of  $g_{\phi r}$ ,  $\chi_{\phi r}$ ,  $\omega_{\mu=2}$  have been verified experimentally for  $H_1$ .

justing the qubit parameters, all circuit parameters are similar in the three circuits. We find that, if the differential capacitance  $C$  and coupling capacitance  $C_c$  are altered such that qubit frequency and qubit-readout coupling are same across all three circuits, the parasitic mode effects are bound to have the same effect given our assumptions of ordered array and no self-nonlinearity in parasitic modes. Hence, we do not expect any change in the MIST/p-MIST effects for single-point connected circuits in the hangar geometry in comparison to what has already been shown in this work. To emphasize this, we plot the three types of coupling strengths across all circuits in Fig. 11(d) while other parasitic parameters are given in Table. IV. Note that, this symmetry prevents any coupling with the lowest-frequency parasitic mode ( $\mu = 1$ ) in all three circuits, presence of which would have been potentially detrimental.

Here we will follow the recipe of Ref. [26] to derive Hamiltonians for circuits shown in Figs. 14(b,c). We will use the following notations defined in Table V. The Lagrangian corresponding to these circuits is a combination of the Lagrangians,  $\mathcal{L}_g$  from the phase-slip junction (comprising of the junction with  $E_J/E_C \sim 5 - 8$  and the capacitor  $C$ ),  $\mathcal{L}_g$  from the ground capacitances,  $\mathcal{L}_{RO}$  from the readout resonator and  $\mathcal{L}_c$  due to the coupling capacitances  $C_c$  and the external voltage  $V$ . We mark the flux points across JJA using  $\varphi_0$  and  $\varphi_N$ . We write the capacitive energy terms using  $E_x = \frac{e^2}{2C_x}$  and the voltages of each island  $\varphi/2e$ , such that,  $\frac{1}{2}C\frac{\dot{\varphi}^2}{4e^2} = \frac{\dot{\varphi}^2}{16E_C}$ . For simplicity, we have  $C_{g,i} = C_g \forall i$ . The flux variables and voltage variables in the circuit are denoted by  $\varphi_n = 2\pi\Phi_n/\Phi_0$  and  $\dot{\varphi}_n = 2\pi V_n/\Phi_0$ , respectively, where  $\Phi_0 = h/2e$  is the superconducting flux quantum. We will use subscripts  $j, p$  for JJA and the phase-slip junction coordinates, respectively. The capacitance associated with the phase-slip junction is given by  $\frac{1}{E_{C'}} = \frac{1}{E_C} + \frac{1}{E_C'}$ .

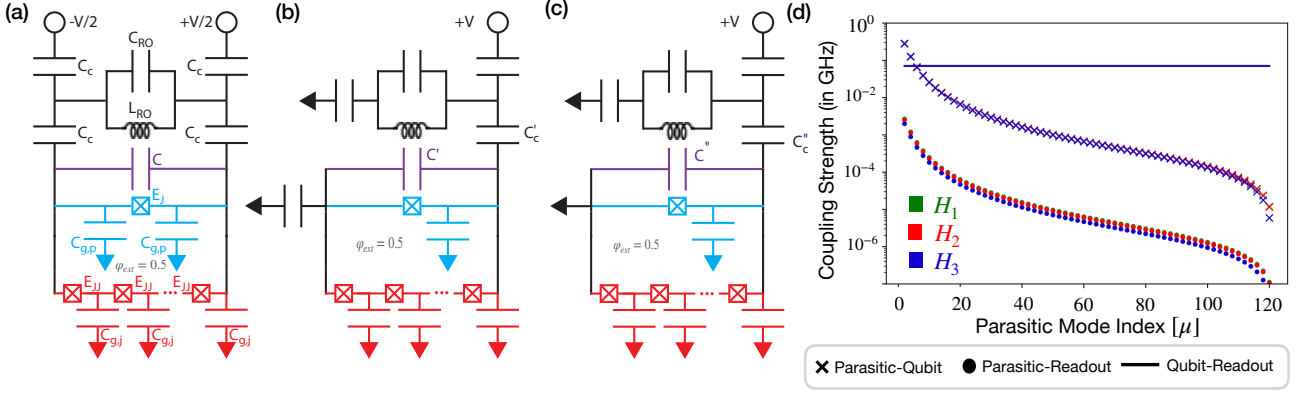


FIG. 11. (a-c) Alternative readout circuits. (a) Parallel circuit, (b) Floating fluxonium, (c) Grounded fluxonium. Alternatives (b) and (c) require a single-point connection to the readout line \$V\$, unlike the parallel circuit in (a). We maintain the values for all circuit variables the same as used for the case of the parallel circuit in Fig. 2. (d) Absolute values of the coefficients of coupling terms in the Hamiltonian (in GHz). We can see that the parasitic modes couple to the qubit stronger than the qubit couples to the readout. The parasitic mode coupling to the readout is very slightly weaker in \$H\_3\$ compared to \$H\_1, H\_2\$.

### 1. Floating Fluxonium Circuit

For \$H\_2\$, Transforming the Lagrangian in Ref. [26], the following terms will remain the same in the case of floating fluxonium circuit, given the diagrams in the following sections.

$$\mathcal{L} = \mathcal{L}_{\text{phase-slip}} + \mathcal{L}_{JJA} + \mathcal{L}_g + \mathcal{L}_{RO} + \mathcal{L}_C \quad (\text{A1})$$

$$\mathcal{L}_{\text{phase-slip}} = \frac{(\dot{\varphi}_N - \dot{\varphi}_0)^2}{16E_{C'}} - E_{J_p} \cos(\varphi_0 - \varphi_N + \varphi_{\text{ext}}) \quad (\text{A2})$$

$$\mathcal{L}_{JJA} = \sum_{n=1}^N \frac{(\dot{\varphi}_n - \dot{\varphi}_{n-1})^2}{16E_{C_j}^n} - E_{J_j}^n \cos(\varphi_n - \varphi_{n-1}) \quad (\text{A3})$$

$$\mathcal{L}_{RO} = \frac{\dot{\varphi}_-^2}{16E_{RO}} - \frac{\varphi_-^2}{16E_{RO}} \quad (\text{A4})$$

$$\mathcal{L}_g = \sum_{n=0}^N \frac{\dot{\varphi}_n^2}{16E_g^n} \quad (\text{A5})$$

Here, we will not assume that the capacitances to transmission line are infinite or that ground capacitance for the phase-slip junction and JJA. We will leave the value of \$\varphi\_{\pm}\$ a variable in this case unlike the parallel circuit study we performed above.

$$\mathcal{L}_c = \frac{(\dot{\varphi}_{-1} - \dot{\varphi}_0)^2}{16E_c^1} + \frac{(\dot{\varphi}_{-1} - eV)^2}{16E_c^3} + \frac{(\dot{\varphi}_{-2})^2}{16E_c^4}, \quad (\text{A6})$$

$$= \frac{\dot{\varphi}_0^2}{16E_c^1} + \frac{\dot{\varphi}_{-1}^2}{16} \left( \frac{1}{E_c^1} + \frac{1}{E_c^3} \right) + \frac{\dot{\varphi}_{-2}^2}{16E_c^4} - \frac{\dot{\varphi}_0 \dot{\varphi}_{-1}}{8E_c^1} - \frac{\dot{\varphi}_{-1} eV}{8E_c^3} + \mathcal{O}(V^2) \quad (\text{A7})$$

Here, \$E\_c^4\$ is the capacitance via which the readout resonator is grounded. Using the basis of (guage-

invariant) phase difference,

$$\varphi_m - \varphi_0 = \sum_{l=1}^m \theta_l \quad (\text{A8})$$

$$\sum_{m=0}^N \theta_m + \varphi_{\text{ext}} = 2\pi z, \quad z \in \mathbb{Z} \quad \text{“fluxoid quantization”} \quad (\text{A9})$$

$$\varphi_{\text{ext}} = \pi, \quad (\text{A10})$$

a. *Lagrangian* From using Eq. A5, we find that,

$$\dot{\varphi}_0 = E_t \left( \frac{\dot{\varphi}_{-1}}{E_c^1} - \sum_{n=1}^N \sum_{m=n}^N \frac{\dot{\theta}_n}{E_g^m} \right) \quad (\text{A11})$$

$$\text{where } E_t = \left( \frac{1}{E_c^1} + \sum_{n=0}^N \frac{1}{E_g^n} \right)^{-1}$$

$$\begin{aligned} \therefore \mathcal{L}_g + \mathcal{L}_c &= \frac{\dot{\varphi}_{-1} eV}{8E_c^3} + \frac{\dot{\varphi}_{-1}^2}{16} \left( \frac{1}{E_c^1} \left( 1 - \frac{E_t}{E_c^1} \right) + \frac{1}{E_c^3} \right) \\ &+ \sum_{n=1}^N \frac{\dot{\varphi}_{-1} \dot{\theta}_n}{E_c^1} \left( \sum_{i=n}^N \frac{E_t}{8E_g^i} \right) \\ &+ \sum_{m=1}^N \sum_{n=1}^N \dot{\theta}_m \dot{\theta}_n \left( \sum_{j=\max\{m,n\}}^N \frac{1}{16E_g^j} \right) \\ &\left( 1 - \sum_{i=\min\{m,n\}}^N \frac{E_t}{E_g^i} \right) \end{aligned} \quad (\text{A12})$$

We simplify the Lagrangian \$\mathcal{L}\_g + \mathcal{L}\_c\$ as

$$\begin{aligned} &= \frac{\dot{\varphi}_{-1} eV}{8E_c^3} + \frac{\dot{\varphi}_{-1}^2}{16} \left( \frac{1}{E_c^1} \left( 1 - \frac{E_t}{E_c^1} \right) + \frac{1}{E_c^3} \right) \\ &+ \sum_{n=1}^N \left( \frac{\dot{\varphi}_{-1} \dot{\theta}_n}{E_c^1} \right) (N - n + 1) \frac{E_t}{8E_g} + \frac{(\dot{\varphi}_{-2})^2}{16E_c^4} \\ &+ \sum_{m=1}^N \sum_{n=1}^N \dot{\theta}_m \dot{\theta}_n \frac{(N - \max\{m,n\} + 1) \min\{m,n\} E_t}{16E_g^2} \end{aligned} \quad (\text{A13})$$



This expansion shows that the parasitic couplings depend on the ground capacitance due to terms like  $\theta_m \dot{\theta}_n$  while the coupling capacitance comes into picture only via couplings with the readout resonator mode.

*b. Collective Modes* We now transform to a new set of variables  $\{\phi, \zeta_1, \dots, \zeta_{N-1}\}$ , also known as the difference modes  $\mu$  and their amplitudes  $\xi_\mu$ ,

$$\theta_m = \phi/N + \sum_{\mu} W_{\mu m} \xi_{\mu}, \quad (\text{A14})$$

and inversely,

$$\phi = \sum_m \theta_m, \quad \xi_{\mu} = \sum_m W_{\mu m} \theta_m. \quad (\text{A15})$$

Here,  $\phi$  is the superinductance mode where all array junction amplitudes are identical. The difference modes  $\xi_{\mu}$  are such that the amplitude sum for all difference modes vanishes. See figures in [15]. The matrix  $(N-1) \times N$  matrix  $W$  is semi-orthogonal,  $\sum_m W_{\mu m} W_{\nu m} = \delta_{\mu\nu}$  and its row sum is zero,  $\sum_m W_{\mu m} = 0$ . Thus, the following choice is observed in [15] and later used in [26]

$$W_{\mu m} = \sqrt{\frac{2}{N}} \cos \frac{\pi \mu (m - 1/2)}{N}. \quad (\text{A16})$$

The choice of these new variables is to identify the collective modes describing the low-energy physics as illustrated in [25, 39, 40]. Thus, under these new set of variables which define the normal modes of oscillations in  $\theta_m$ , we have,

$$\mathcal{L} = \mathcal{T} - \mathcal{U} \quad (\text{A17})$$

$$\begin{aligned} \mathcal{T} = & \frac{\dot{\varphi}_{-1} eV}{8E_c^3} - \frac{\dot{\varphi}_{-2} eV}{8E_c^4} - E_t \frac{\dot{\varphi}_{-1} \dot{\varphi}_{-2}}{8E_c^2} \\ & + \frac{\dot{\varphi}_{-1}^2}{16} \left( \frac{1}{E_c} \left( 1 - \frac{E_t}{E_c} \right) + \frac{1}{E_c^3} \right) + \frac{\dot{\varphi}_{-2}^2}{16} \left( \frac{1}{E_c^4} + \frac{1}{E_c} \left( 1 - \frac{E_t}{E_c} \right) \right) \\ & + \left[ \sum_{n=1}^N \left( \frac{\dot{\varphi}_{-1}}{E_c} + \frac{\dot{\varphi}_{-2}}{E_c} \right) \left( \frac{E_t}{8E_c} + (N-n+1) \frac{E_t}{8E_g} \right) \right. \\ & \quad \left. - \sum_{n=1}^N \frac{\dot{\varphi}_{-2}}{8E_c} \right] (\dot{\phi}/N + \sum_{\mu} W_{\mu n} \dot{\xi}_{\mu}) + \sum_{m=1}^N \sum_{n=1}^N (\dot{\phi}/N \\ & + \sum_{\mu} W_{\mu n} \dot{\xi}_{\mu}) (\dot{\phi}/N + \sum_{\mu} W_{\mu m} \dot{\xi}_{\mu}) \left( (N - \max\{m, n\} \right. \\ & \quad \left. + 1) \frac{1}{16E_g} + \frac{1}{16E_c} \right) \left( \min\{m, n\} \frac{E_t}{E_g} + \frac{E_t}{E_c} \right) \quad (\text{A18}) \end{aligned}$$

$$\begin{aligned} \mathcal{U} = & -E_{J_p} \cos(\phi) - \frac{(\varphi_{-1} - \varphi_{-2})^2}{16E_{RO}} \\ & - \sum_{n=1}^N E_{J_j} \cos \left( \phi/N + \sum_{\mu} W_{\mu n} \xi_{\mu} \right) \quad (\text{A19}) \end{aligned}$$

*c. Symmetries in the Lagrangian* Simplifying the kinetic energy term from Eq. A18 using  $\sum_m W_{\mu m} = 0$  and the semi-orthogonal matrix con-

dition  $\sum_m W_{\mu m} W_{\nu m} = \delta_{\mu\nu}$  used above yields,

$$\begin{aligned} \mathcal{T} = & -\frac{\dot{\varphi}_{-2} eV}{16E_c} + \frac{\dot{\varphi}_{-1} eV}{16E_c} - E_t \frac{\dot{\varphi}_{-1} \dot{\varphi}_{-2}}{16E_c^2} \\ & + \frac{\dot{\varphi}_{-1}^2}{16} \left( \frac{1}{E_c} \left( 1 - \frac{E_t}{E_c} \right) + \frac{1}{E_c} \right) + \frac{\dot{\varphi}_{-2}^2}{16} \left( \frac{1}{E_c} + \frac{1}{E_c} \left( 1 - \frac{E_t}{E_c} \right) \right) \\ & + \frac{E_t}{8E_c^2} \dot{\varphi}_{-1} \dot{\phi} + \frac{E_t}{8E_c^2} \dot{\varphi}_{-2} \dot{\phi} \\ & + \left[ \sum_{n=1}^N \left( \frac{\dot{\varphi}_{-1}}{E_c} + \frac{\dot{\varphi}_{-2}}{E_c} \right) \left( \frac{E_t}{8E_c} + (N-n+1) \frac{E_t}{8E_g} \right) \right. \\ & \quad \left. - \sum_{n=1}^N \frac{\dot{\varphi}_{-2}}{8E_c} \right] (\dot{\phi}/N + \sum_{\mu} W_{\mu n} \dot{\xi}_{\mu}) \\ & + \left[ (M_{00} + G_{00}) \dot{\phi}^2 + 2 \sum_{\mu} (M_{0\mu} + G_{0\mu}) \dot{\phi} \dot{\xi}_{\mu} \right. \\ & \quad \left. + \sum_{\mu, \nu} (M_{\mu\nu} + G_{\mu\nu}) \dot{\xi}_{\mu} \dot{\xi}_{\nu} \right] \quad (\text{A20}) \end{aligned}$$

Here  $M$  comes from the phase-slip junction and JJA while  $G$  comes from the coupling and ground capacitances, and these coefficients are given by,

$$M_{00} = \frac{1}{16E_{C'}} + \frac{1}{16NE_{C_j}}, \quad M_{0\mu} = 0, \quad M_{\mu\nu} = \frac{\delta_{\mu\nu}}{16E_{C_j}} \quad (\text{A21})$$

$$G_{00} = \frac{1}{64E_t} \left( 1 - \frac{E_t}{E_c} \right)^2 \left[ 1 - \frac{2}{3} \frac{N-1}{N} \right] \quad (\text{A22})$$

$$G_{0\mu} = -\frac{c_{\mu} o_{\mu+1}}{16E_g \sqrt{2N} s_{\mu}^2} \left( 1 - \frac{E_t}{E_c} \right) \quad (\text{A23})$$

$$G_{\mu\nu} = \frac{1}{64E_g s_{\mu}^2} \left[ \delta_{\mu\nu} - \frac{E_t}{E_g} \frac{2c_{\mu} c_{\nu} o_{\mu} o_{\nu}}{N s_{\nu}^2} \right] \quad (\text{A24})$$

$$\text{where } E_t = \left( \frac{1}{E_c} + \sum_{n=0}^N \frac{1}{E_g^n} \right)^{-1}$$

Here  $G_{00}$  increases quadratically with a factor of  $\left( 1 - \frac{E_t}{E_c} \right)$ . Thus,  $G_{0\mu}$  is different from the parallel circuit by a factor  $\left( 1 - \frac{E_t}{E_c} \right)$ . For the last term,  $G_{\mu\nu}$ , it is the same as parallel circuit because there is no term dependent on  $E_c$ .

*d. Linear Approximation* From here on, the sum over  $m, n$  runs from 1 to  $N$  while the sum over  $\mu, \nu$  runs from 1 to  $N-1$ . Simplification to including only linear terms from Taylor expansion of the cosine ( $\cos x \sim 1 - \frac{x^2}{2}$ ) Eq. A19 and using  $\sum_n W_{\mu n} W_{\nu n} = \delta_{\mu\nu}$ , yields (upto a constant term)

$$\begin{aligned} \mathcal{U} = & E_{J_p} \cos(\phi) - \frac{(\varphi_{-1} - \varphi_{-2})^2}{16E_{RO}} \\ & + \frac{E_{J_j}}{2N} \phi^2 + \frac{E_{J_j}}{2} \sum_{\mu} \xi_{\mu}^2 \quad (\text{A25}) \end{aligned}$$

$$= E_{J_p} \cos(\phi) + \frac{E_{J_j}}{2N} \phi^2 + \frac{E_{J_j}}{2} \sum_{\mu} \xi_{\mu}^2 - \frac{\varphi_{-2}^2}{16E_{RO}}, \quad (\text{A26})$$

where  $\dot{\phi}_{-1} = -\dot{\phi}_{-2} = eV$

*e. Hamiltonian:* We can see that there is no choice of  $\dot{\varphi}_\pm$  such that the parasitic coupling between the readout resonator and fluxonium can be cancelled without eliminating the coupling between the qubit and readout resonator. Note that, this expression assumed  $C_g^0 = C_g^N = C_g^1 = C_g^{N-1}$ , such that  $\frac{N+1}{E_g} = \frac{1}{E_g} - \frac{1}{E_c}$ . The coupling between the qubit and the readout is same as the parallel circuit if  $E_g \ll E_c$  with a lower  $N$ . We drive the readout resonator, such that,  $\dot{\varphi}_- = 2eV$  (the sign of the voltage value has been changed because in this circuit  $\varphi_{-1}$  will be connected to  $V$  and not  $-V$ , just for simplicity). [SS: Check the sign of the eV terms]

$$\begin{aligned} \mathcal{L} = & \frac{\dot{\varphi}_+^2}{64E_c} \left( 2 + \frac{(N+1)E_t}{E_g} \right) + \frac{\dot{\varphi}_+ eV}{16E_c} \left( \frac{3}{2} + \frac{E_t}{E_c} \right) \\ & - \frac{(N+1)E_t}{32E_g E_c} \dot{\varphi}_+ eV + \frac{(N+1)E_t}{64E_g E_c} \dot{\varphi}_+ \dot{\varphi}_+ \\ & - \frac{E_t}{16E_g E_c} \sum_\mu \frac{c_\mu o_\mu}{\sqrt{2N}s_\mu^2} \dot{\xi}_\mu eV \\ & + \frac{E_t}{32E_g E_c} \sum_\mu \frac{c_\mu o_\mu}{\sqrt{2N}s_\mu^2} \dot{\xi}_\mu \dot{\varphi}_+ \mathcal{O}(e^2 V^2) \\ & + \left[ (M_{00} + G_{00}) \dot{\varphi}^2 + 2 \sum_\mu (M_{0\mu} + G_{0\mu}) \dot{\varphi} \dot{\xi}_\mu \right. \\ & \left. + \sum_{\mu,\nu} (M_{\mu\nu} + G_{\mu\nu}) \dot{\xi}_\mu \dot{\xi}_\nu \right] - \mathcal{U} \end{aligned} \quad (\text{A27})$$

This Lagrangian can be used to analyze effects in floating readout case. However, for simplicity, we can again just like the previous case, assume  $C^3 = C^4 = 0$  which makes the floating resonator grounded. Ideally this choice should not affect the analysis until we study the effects of a driven readout resonator (even then the intuition is that the ground capacitance should not make things worse [SS: Check this intuition when analyzing a driven resonator. Also, we can check if changing  $C_g^N = E_c^2 = E + C^1$  brings the effect of Floating resonator closer to a parallel circuit. It will never be similar because we have one less ground capacitance term here.]). Currently this is equivalent to eliminating all terms with  $E_c^3, E_c^4$  and using  $\dot{\varphi}_{-2} = 0, \dot{\varphi}_{-1} = -2eV$ . Thus,  $\varphi_+ = \varphi_- = -2eV$ .

$$\begin{aligned} = & - \frac{(N+1)E_t}{16E_g E_c} \dot{\varphi}_+ eV - \frac{E_t}{8E_g E_c} \sum_\mu \frac{c_\mu o_\mu}{\sqrt{2N}s_\mu^2} \dot{\xi}_\mu eV \\ & + \left[ (M_{00} + G_{00}) \dot{\varphi}^2 + 2 \sum_\mu (M_{0\mu} + G_{0\mu}) \dot{\varphi} \dot{\xi}_\mu \right. \\ & \left. + \sum_{\mu,\nu} (M_{\mu\nu} + G_{\mu\nu}) \dot{\xi}_\mu \dot{\xi}_\nu \right] - \mathcal{U} \end{aligned} \quad (\text{A28})$$

Next, we write the Legendre transformation using the velocity vectors and matrices,

$$\begin{aligned} p_\phi &= \frac{\partial \mathcal{L}_{\mathcal{K}_o}}{\partial \dot{\varphi}} = 2(M_{00} + G_{00}) \dot{\varphi} + \sum_\mu (M_{\mu 0} + G_{\mu 0}) \dot{\xi}_\mu \\ & - \frac{(N+1)E_t}{16E_g E_c} eV \\ p_{\xi_\mu} &= \frac{\partial \mathcal{L}_{\mathcal{K}_o}}{\partial \dot{\xi}_\mu} = (M_{0\mu} + G_{0\mu}) \dot{\varphi} + 2 \sum_\nu (M_{\mu\nu} + G_{\mu\nu}) \dot{\xi}_\nu \end{aligned} \quad (\text{A29})$$

$$- \frac{E_t}{8E_g E_c} \sum_\mu \frac{c_\mu o_\mu}{\sqrt{2N}s_\mu^2} eV \quad (\text{A30})$$

Here, the even and odd sectors are not decoupled due to the  $eV$  term which will eventually act as the readout resonator mode. The even and odd sectors can be diagonalized independently, such that a rotation on the odd sectors does not affect the even sectors. This is contrary to the case of Eq. 77 in [26] where the rotation of odd sectors affects the even sectors. This is because in that case  $G_{0\mu}$  was changed to being dependent on odd as well as even sectors. However, here, only the  $\mathcal{L}_V$  term has changed. Thus, if the following condition is satisfied,

$$\frac{\tilde{E}_c^\phi \tilde{E}_{c,j}^e c_i c_j}{32N E_g^2 s_i^2 s_j^2} \ll 1 \implies \frac{4E_g \tilde{E}_c^\phi c_i c_j}{32N E_g^2 s_i^2} \ll 1 \quad (\text{A31})$$

$$\implies \frac{4\tilde{E}_c^\phi N}{8E_g \pi^2 \mu\nu} \ll 1 \implies N \ll 8\pi^2 \frac{E_g}{\tilde{E}_c^\phi} \quad (\text{A32})$$

we can carry out the exact same procedure as Ref. [26] to simplify the inversion of matrix for the Legendre transformation and obtain the Hamiltonian as follows. [SS: Check both the matrix inverse requirement and condition in this case again]. Thus, we get the Hamiltonian as,

$$\begin{aligned} H_2 = & 4\tilde{E}_c^\phi p_\phi^2 + \sum_{\mu=1}^{N-1} 4\tilde{E}_{c,\mu}^{e/o} p_\mu^2 \\ & + 2 \sum_{\mu=1}^{N-1} \frac{\tilde{E}_c^\phi \tilde{E}_{c,\mu}^{e/o} c_\mu o_{\mu+1}}{\sqrt{2N} E_g s_\mu^2} p_\phi p_\mu \\ & - \tilde{E}_c^\phi p_\phi eV \left[ \frac{(N+1)E_t}{2E_g E_c} + \frac{E_t \tilde{E}_{c,\mu}^{e/o}}{8E_g^2 E_c^2} \left( \frac{c_\mu^2 o_\mu}{2N s_\mu^4} \right) \right] \\ & - \sum_{\mu=1}^{N-1} \frac{\tilde{E}_c^\phi \tilde{E}_{c,\mu}^{e/o} c_\mu o_{\mu+1}}{\sqrt{2N} E_g s_\mu^2} \left[ \frac{(N+1)E_t}{8E_g E_c} \right] p_\mu eV \\ & + E_{J_p} \cos \phi + \frac{E_L}{2} \phi^2 + \frac{E_{J_j}}{2} \sum_{\mu=1}^{N-1} \xi_\mu^2 - \frac{\varphi_-^2}{16E_{RO}} \end{aligned} \quad (\text{A33})$$

where the variables  $\tilde{E}_{c,\mu}^e$  are same as before and  $\tilde{E}_{c,\mu}^o$  is the diagonalized charging energy of odd sectors.  $\tilde{E}_{c,\mu}^{e/o}$  denotes that the term will be  $\tilde{E}_{c,\mu}^o$  for odd  $\mu$  and  $\tilde{E}_{c,\mu}^e$  for even  $\mu$ . Thus, we can see that by not preserving the symmetry we only have the extra odd sector term interacting with the readout resonator. However, we can see that this term is extremely small.  $\mathcal{U}$  remains the same as the parallel case. Thus, in terms of types of couplings there might not be major differences, however, value of  $\tilde{E}_c^\phi = (G_{00} + M_{00})^{-1}$  changes since  $G_{00}$  has changed. This change can also be diminished with increasing  $N$ . Thus, for large enough  $N$ , this circuit is the same as the parallel circuit. [SS: Write this in terms of previous format of  $H_\phi$ ]

## 2. Grounded Fluxonium Circuit

For  $H_3$ , the constraint  $\dot{\varphi}_N = 0$  yields

$$\mathcal{L} = \mathcal{L}_{\text{phase-slip}} + \mathcal{L}_{JJA} + \mathcal{L}_g + \mathcal{L}_{RO} + \mathcal{L}_C \quad (\text{A34})$$

$$\mathcal{L}_{\text{phase-slip}} = \frac{\dot{\varphi}_0^2}{16E_{C'}} - E_{J_p} \cos(\varphi_0 + \varphi_{ext}) \quad (\text{A35})$$

$$\mathcal{L}_{JJA} = \sum_{n=1}^N \frac{(\dot{\varphi}_n - \dot{\varphi}_{n-1})^2}{16E_{C_j}^n} - E_{J_j}^n \cos(\varphi_n - \varphi_{n-1}) \quad (\text{A36})$$

$$\mathcal{L}_{RO} = \frac{\dot{\varphi}_-^2}{16E_{RO}} - \frac{\varphi_-^2}{16E_{RO}} \quad (\text{A37})$$

$$\mathcal{L}_g = \sum_{n=0}^{N-1} \frac{\dot{\varphi}_n^2}{16E_g^n} \quad (\text{A38})$$

Here, we will not assume that the capacitances to transmission line are infinite or that ground capacitance for the phase-slip junction and JJA. We will leave the value of  $\varphi_{\pm}$  a variable in this case unlike the parallel circuit study we performed above. The grounding of fluxonium yields an additional condition to the fluxoid condition  $\varphi_N = c$ , a constant which implies,

$$\varphi_0 = c - \sum_{l=1}^N \theta_l \implies \dot{\varphi}_0 = - \sum_{l=1}^N \dot{\theta}_l \quad (\text{A39})$$

This used to be our qubit in the definition of collective modes in this article. However, in this case there are only  $N-1$  modes, such that the collective modes are defined as,

$$\phi = c + \sum_{l=1}^{N-1} \theta_l \implies \dot{\phi} = -\dot{\varphi}_0 \quad (\text{A40})$$

[SS: Is there a different mechanism we need to use here? (1) We should only have N-1 modes] Since one of the dynamic variables are fixed we only have  $N-1$  modes, thus,

$$\mathcal{L}_{\text{phase-slip}} = \frac{(\sum_{m=1}^{N-1} \dot{\theta}_m)^2}{16E_{C'}} + E_{J_p} \cos\left(\sum_{m=1}^N \theta_m + \varphi_{ext}\right) \quad (\text{A41})$$

$$\mathcal{L}_{JJA} = \sum_{n=1}^{N-1} \frac{\dot{\theta}_n^2}{16E_{C_j}^n} - E_{J_j}^n \cos \theta_n \quad (\text{A42})$$

$$\mathcal{L}_{RO} = \frac{(\dot{\varphi}_{-1} - \dot{\varphi}_{-2})^2}{16E_{RO}} - \frac{(\varphi_{-1} - \varphi_{-2})^2}{2L_{RO}} \quad (\text{A43})$$

$$\mathcal{L}_g = \frac{\dot{\varphi}_0^2}{16E_g^0} + \sum_{n=1}^N \frac{(\dot{\varphi}_0 + \sum_{m=1}^n \dot{\theta}_m)^2}{16E_g^n} \quad (\text{A44})$$

$$= \frac{\dot{\varphi}_0^2}{16E_g^0} + \sum_{n=1}^N \frac{1}{16E_g^n} (\dot{\varphi}_0^2 + 2\dot{\varphi}_0 \sum_{m=1}^n \dot{\theta}_m + \sum_{i=1}^n \sum_{j=1}^n \dot{\theta}_i \dot{\theta}_j) \quad (\text{A45})$$

$$= \dot{\varphi}_0^2 \sum_{n=0}^N \frac{1}{16E_g^n} + 2 \sum_{n=1}^N \sum_{m=1}^n \frac{\dot{\varphi}_0 \dot{\theta}_m}{16E_g^n} + \sum_{n=1}^N \sum_{j=1}^n \sum_{i=1}^n \frac{\dot{\theta}_i \dot{\theta}_j}{16E_g^n} \quad (\text{A46})$$

$$\begin{aligned} \mathcal{L}_c = & \frac{\dot{\varphi}_0^2}{16E_c^1} + \frac{\dot{\varphi}_{-1}^2}{16} \left( \frac{1}{E_c^1} + \frac{1}{E_c^3} \right) \\ & + \frac{\dot{\varphi}_{-2}^2}{16} \left( \frac{1}{E_c^4} + \frac{1}{E_c^2} \right) + \frac{(\dot{\varphi}_0 + \sum_{m=1}^N \dot{\theta}_m)^2}{16E_c^2} \\ & - \frac{\dot{\varphi}_0 \dot{\varphi}_{-1}}{8E_c^1} - \frac{\dot{\varphi}_{-2}(\dot{\varphi}_0 + \sum_{m=1}^N \dot{\theta}_m)}{8E_c^2} \\ & - \frac{\dot{\varphi}_{-2}eV}{8E_c^4} + \frac{\dot{\varphi}_{-1}eV}{8E_c^3} \end{aligned} \quad (\text{A47})$$

The term  $\frac{(\dot{\varphi}_{-2})^2}{16E_c^4}$  will be added to the Lagrangian. The coupling constant for this case is,

$$\mathcal{L}_c = \frac{(\dot{\varphi}_{-1} - \dot{\varphi}_0)^2}{16E_c^1} + \frac{(\dot{\varphi}_{-1} - eV)^2}{16E_c^3} + \frac{(\dot{\varphi}_{-2})^2}{16E_c^4}, \quad (\text{A48})$$

$$\begin{aligned} \mathcal{L} = & \frac{\dot{\varphi}_+^2}{16E_c} \left( 2 + \frac{NE_t}{E_g} \right) - \frac{\dot{\varphi}_+ eV}{4E_c} \left( \frac{3}{8} + \frac{E_t}{E_c} \right) \\ & - \frac{NE_t}{16E_g E_c} \dot{\phi} eV - \frac{NE_t}{32E_g E_c} \dot{\phi} \dot{\varphi}_+ \end{aligned} \quad (\text{A49})$$

$$\begin{aligned} & - \frac{E_t}{8E_g E_c} \sum_{\mu} \frac{c_{\mu} o_{\mu}}{\sqrt{2(N-1)} s_{\mu}^2} \dot{\xi}_{\mu} eV \\ & - \frac{E_t}{8E_g E_c} \sum_{\mu} \frac{c_{\mu} o_{\mu}}{\sqrt{2(N-1)} s_{\mu}^2} \dot{\xi}_{\mu} \dot{\varphi}_+ + \mathcal{O}(e^2 V^2) \end{aligned} \quad (\text{A50})$$

$$\begin{aligned} & + \left[ (M_{00} + G_{00}) \dot{\phi}^2 + 2 \sum_{\mu} (M_{0\mu} + G_{0\mu}) \dot{\phi} \dot{\xi}_{\mu} \right. \\ & \left. + \sum_{\mu, \nu} (M_{\mu\nu} + G_{\mu\nu}) \dot{\xi}_{\mu} \dot{\xi}_{\nu} \right] - \mathcal{U} \end{aligned} \quad (\text{A51})$$

*a. Hamiltonian:* All terms in the Hamiltonian ( $H_2$ ) can be adopted via  $N \rightarrow N-1$ . If  $C_g^N \neq C_g^1$  then this ground fluxonium and floating fluxonium have a larger difference in terms of frequencies of modes.

## Appendix B: Undriven Fluxonium Circuit

In this appendix, we give the details of calculation and values (see Table V) of the measurement circuit in Fig. 2(a). The Hamiltonian for this circuit was derived in [26]. In addition, we also give some calculations post Hamiltonian derivation of the single-point connection circuits, shown in Fig. 11(b,c). For Hamiltonian derivations of these circuit, see Sec. A. Throughout the document we quote energies in units of  $h$  i.e. GHz. We assume,

- $N = 122$
- $C_g^0 = C_g^N \neq C_g^i \quad \forall i \in [1, 2, \dots, N-1]$ .
- capacitance between the transmission line and readout resonator is infinite, such that the readout resonator is at voltage  $V$ .

General Fluxonium Circuit	Phase-Slip Junction	Josephson-Junction Array
Ground capacitance	$C_g^0 = C_g^N = 10 - 20 fF$	$\{C_g^1, \dots, C_g^{N-1}\} = 0.05 - 0.1 fF$
Josephson Junction Energy	$E_{J_p} = 5 - 20 \text{GHz}$	$E_{J_j} = 40 - 100 \text{GHz}$
Capacitance Energy	$E_{C'} = 1 - 4 \text{GHz}$	$E_{C_j} = 50 fF / 115 E_{J_p} \text{GHz}$

Readout Circuit Parameters	Variables	Values
Readout Frequency	$\omega_r / 2\pi$	6-9 GHz
Resonator kappa	$\kappa_r$	1-15MHz (easy to tune)
Readout Impedance	$Z(\omega)$	$100/\pi$ or $200/\pi$
qubit-RO Coupling Capacitance (left)	$C_{c,1}$	1-2fF (Easy to tune)
qubit-RO Coupling Capacitance (right)	$C_{c,2}$	1-2fF (Easy to tune)
qubit frequency	$\omega_{01}$	33.7MHz
plasmon frequency	$\omega_{12}$	6.082GHz
dispersive shift (readout resonator)	$\chi_{RO}$	0.5MHz for $g=20\text{MHz}$
Zero-point fluctuation of charge of resonator	$\phi_{r,ZPF}$	2.84
$T_2^*$ limitation from 50mK resonator	$T_2$	8.9ms
coupling coefficient	$g_{r,\phi}$	26.1MHz
dispersive shift	$\chi_{01}$	0.38MHz
dispersive shift	$\chi_{12}$	0.125MHz
self-kerr	$K_r$	0.001MHz (averaged upto 10 photons)

Parameters	Variables	Set 1
Number of junctions in the array	$N$	122
Phase-Slip JJ energy	$E_{J_p}$	7.3 GHz
Target capacitance	$e^2/2(C_g + C')$	1GHz
Phase-Slip junction capacitance+differential capacitance	$E_{C'}$	$(1 - 2/E_{g,p})^{-1} \text{GHz}$
JJA junction energy	$E_{J_j}$	60 GHz
JJA capacitance energy	$E_{C_j}$	0.74GHz
JJA ground capacitance	$E_{g,j}$	194 GHz
Phase-slip parasitic ground capacitance	$E_{g,p}$	1.94 GHz
Coupling capacitance	$E_c$	19.4 GHz
Readout loss rate	$\kappa_r$	1MHz
Readout Frequency	$\omega_r / 2\pi$	8.5GHz
Quality-Factor	$Q$	8500
Zero-point fluctuation of charge operator	$n_{ZPF}$	1.4
Zero-point fluctuation of phase operator	$\phi_{ZPF}$	0.357

TABLE V. Circuit Parameters. Capacitive energies  $E_g, E_c$ , etc.. are determined using  $E_c = (e^2/2hC) = \frac{1.94e-5}{C} = 19.4/C(fF)[\text{GHz}]$ .

### 1. Circuit Features

- **Zero-point fluctuation of  $e\hat{V}/h$ :** We can use  $eV = 2e^2(n_r/\sqrt{2})/C_r = 4E_{C_r}(n_r/\sqrt{2})$ . If we absorb the factor of  $4E_{C_r}$  in the coupling coefficient, then  $\frac{n_{ZPF}}{\sqrt{2}} = \left(\frac{E_L}{8E_{C_r}}\right)^{1/4}$  and  $e\hat{V} = 4E_{C_r}\hat{n}$ . This is exactly equal to the quantity in Table V [41].
- **Zero-point fluctuation of  $n_{\phi,r}$ :** For the qubit mode, we use the harmonic oscillator approximation where we define,  $\frac{n_{ZPF}}{\sqrt{2}} = \left(\frac{E_J^j}{8NE_C^{\phi}}\right)^{1/4} = 1/\phi_{ZPF} \approx 0.36(H_1), 0.34(H_2), 0.34(H_3)$ . This approximation holds correct if the convergence is taken care of using proper cutoff on this basis.
- **Zero-point fluctuation of  $n_{\mu,r}$ :** For parasitic modes, it is  $n_{ZPF} = \left(\frac{E_J^j}{8E_{C,\mu}^e}\right)^{1/4}$ . We could use this to compute the absolute strengths for parasitic modes and resonator couplings.
- **Occupation Number of the Parasitic**

**Modes:** As discussed in the main text, the parasitic mode frequencies are given by,

$$\omega_{\mu}^o = \sqrt{8E_{c,\mu}^o E_{J_j}} \quad (\text{B1})$$

$$\omega_{\mu}^e = \sqrt{8E_{c,\mu}^e E_{J_j}} \quad (\text{B2})$$

Here we have expressed  $\omega$  for the case when energies are expressed in GHz. The thermal population of the parasitic modes can be calculated as  $n = \frac{1}{e^{hf/kT} - 1}$  where  $k, T, f$  are the Boltzmann constant, temperature, and mode frequency, respectively. The frequency curve shown in Fig. 2 saturates at 18.8 GHz while the occupation number of the lowest even (odd) mode stands at 12.06 (7.25). Only the even modes couple to the readout and parasitic modes. The occupation number of the first even (odd) mode is  $9.3e - 6$  ( $9e - 4$ ). The highest mode saturates at an occupation number of  $1.4e - 8$ . Importantly, For a temperature of  $20mK$ , the lowest odd mode population is down to  $6.3e - 8$ .

1. Total ground capacitance.



- (a)  $H_1 : E_t = \left(\frac{N-1}{E_g} + \frac{2}{E_{g1}} + \frac{2}{E_c}\right)^{-1} = 0.57\text{GHz}$   
 (b)  $H_2 : E_t = \left(\frac{N-1}{E_{gj}} + \frac{2}{E_{gp}} + \frac{1}{E_c}\right)^{-1}$   
 (c)  $H_3 : E_t = \left(\frac{N-1}{E_{gj}} + \frac{1}{E_{gp}} + \frac{1}{E_c}\right)^{-1}$

## 2. Qubit Charging energy ( $4E_c^\phi \hat{N}_\phi^2$ ).

- (a)  $H_1 : \bar{E}_c^\phi = \left(\frac{1}{4E_t} \left(1 - \frac{2}{3} \frac{(N+1)(N-1)}{N} \frac{E_t}{E_g}\right) + \frac{1}{E_{c'}} + \frac{1}{NE_{c_j}}\right)^{-1} = 0.92 \text{ GHz}.$   
 (b)  $H_2 : \bar{E}_c^\phi = \left(\frac{1}{4E_t} \left(1 - \frac{E_t}{E_c}\right)^2 \left[1 - \frac{2}{3} \frac{N-1}{N}\right] + \frac{1}{E_{c_p}} + \frac{1}{NE_{c_j}}\right)^{-1}.$   
 (c)  $H_3 : \bar{E}_c^\phi = \left(\frac{1}{4E_t} \left(1 - \frac{E_t}{E_c}\right)^2 \left[1 - \frac{2}{3} \frac{N-2}{N-1}\right] + \frac{1}{E_{c_p}} + \frac{1}{NE_{c_j}}\right)^{-1}.$

## 3. Even Parasitic Mode Charging Energy ( $4E_{c,\mu}^e \hat{N}_\mu^2$ ).

- (a)  $H_1 : \tilde{E}_{c,\mu}^e = \left(\frac{1}{E_{c_j}} + \frac{1}{4E_g s_\mu^2}\right)^{-1}$   
 (b)  $H_2 : \text{Same as } H_1$   
 (c)  $H_3 : \text{Same as } H_1$

## 4. Qubit-Readout Coupling ( $g_{\phi r} \hat{N}_\phi \hat{N}_\mu$ ).

- (a)  $H_1 : \frac{\bar{E}_c^\phi}{E_c}$   
 (b)  $H_2 : \frac{\bar{E}_c^\phi}{E_c} \left[ \frac{(N+1)E_t}{2E_{gj}} + \frac{E_t^2 \bar{E}_{c,\mu}^e}{8E_{gj}^2 E_c} \left(\frac{c_\mu^2}{2Ns_\mu^4}\right) \right]$   
 (c)  $H_3 : \frac{\bar{E}_c^\phi}{E_c} \left[ \frac{NE_t}{2E_{gj}} + \frac{E_t^2 \bar{E}_{c,\mu}^e}{8E_{gj}^2 E_c} \left(\frac{c_\mu^2}{2(N-1)s_\mu^4}\right) \right]$

## 5. Qubit-Parasitic Coupling ( $g_{\phi\mu} \hat{N}_\phi \hat{N}_\mu$ ).

- (a)  $H_1 : \sqrt{\frac{2}{N}} \frac{\bar{E}_c^\phi \bar{E}_{c,\mu}^e c_\mu}{E_{gj} s_\mu^2}$   
 (b)  $H_2 : \sqrt{\frac{2}{N}} \frac{\bar{E}_c^\phi \bar{E}_{c,\mu}^e c_\mu}{E_{gj} s_\mu^2}$   
 (c)  $H_3 : \sqrt{\frac{2}{N-1}} \frac{\bar{E}_c^\phi \bar{E}_{c,\mu}^e c_\mu}{E_{gj} s_\mu^2}$

## 6. Readout-Parasitic Coupling ( $g_{\mu r} \hat{N}_\mu \hat{N}_r$ ).

- (a)  $H_1 : \frac{\bar{E}_c^\phi \bar{E}_{c,\mu}^e c_\mu}{4\sqrt{2N} E_{gj} E_c s_\mu^2}$   
 (b)  $H_2 : \frac{\bar{E}_c^\phi \bar{E}_{c,\mu}^e c_\mu}{4\sqrt{2N} E_{gj} s_\mu^2 E_c} \left[ \frac{(N+1)E_t}{2E_g} \right]$   
 (c)  $H_3 : \frac{\bar{E}_c^\phi \bar{E}_{c,\mu}^e c_\mu}{4\sqrt{2(N-1)} E_{gj} s_\mu^2 E_c} \left[ \frac{NE_t}{2E_{gj}} \right]$

## 2. Qubit Hamiltonian

The qubit Hamiltonian  $H_\phi$  is diagonalized in the Fock state basis, where we have used  $\hat{x} = x_{zpf}(a + a^\dagger)$  and  $\hat{p} = -ip_{zpf}(a - a^\dagger)$ , then  $x_{zpf} = \frac{1}{2p_{zpf}}$ . Each zero-point fluctuation value in the two cases is related as  $ZPF_2 = ZPF_1/\sqrt{2}$ .

*a. Energy Spectrum for  $H_1$ :* The Hamiltonian of the qubit subspace is  $H_\phi = 4\tilde{E}_C^\phi n_\phi^2 + E_{J,p} \cos \phi + \frac{1}{2} E_L \phi^2$ , where  $E_L = \frac{E_J}{N}$ . The zero-point fluctuation of the unit-less phase operator  $\phi$  is  $n_{ZPF,\phi}^{-1} = 1.39$ .

*b. Charge Matrix Elements for  $H_1, H_2, H_3$ :* Here, using the approximations described in the appendix, we get the following charge matrix elements for the qubit subspace.

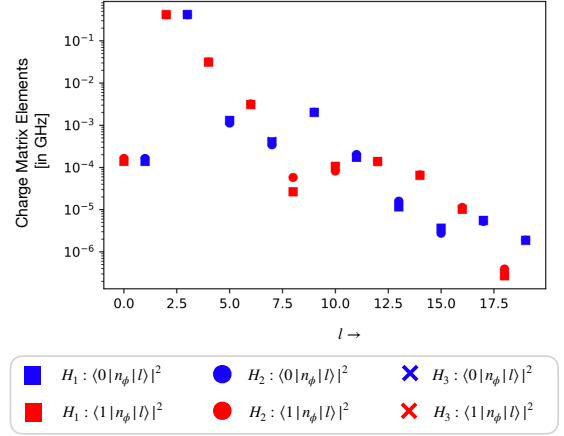


FIG. 12. Charge Matrix Elements (squared) for all three circuits. Note that in the equations below we substitute  $\langle l|n|l' \rangle = in_{ZPF} \langle l|a - a^\dagger|l' \rangle$  where  $n_{ZPF} = \frac{1}{\sqrt{2}} \left( E_{J,j} / 8NE_c \right)^{1/4}$ . The charge matrix elements between odd-odd or even-even is zero (points not seen in log plot) due to the symmetry of cosine potential at  $\varphi_{ext} = 0.5\Phi_0$ , where  $\Phi_0$  is the flux quantum.

*c. Coupling Constant Landscape:* The coupling constants decrease with increasing  $\mu$ . We plot the coupling constants for the parallel circuit named  $H_1$  in Fig. 2 of the main text in Fig. 13. In addition, we give coupling constants of the single-point connection circuits, elaborated in Sec. A.

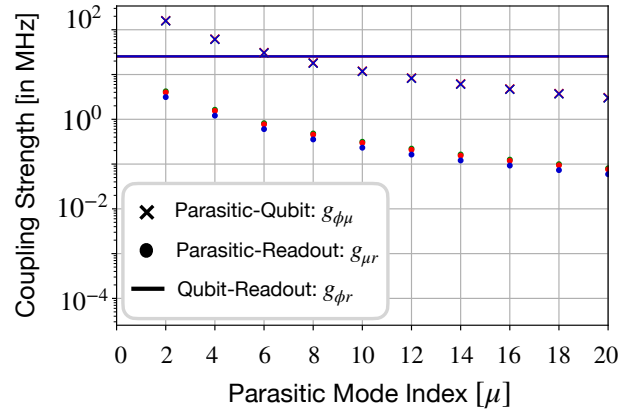


FIG. 13. Absolute values of the coupling strengths in GHz for various circuits.  $H_1$  (green): Parallel circuit (see Fig. 2),  $H_2$  (blue): single-Point connection with floating fluxonium (see Fig. 11 (b)), and  $H_3$  (red): single-Point Connection with grounded fluxonium (see Fig. 11 (c)). The behavior for all circuits is the same, thus the discussion in the main text focused on  $H_1$  can be easily extended to  $H_2, H_3$ . Coupling to odd parasitic modes is zero due to the symmetries of the circuit [26].

Below in Fig. 14 is the dependence of charging energies and coupling constants on the number of junctions as well as the ground capacitance.

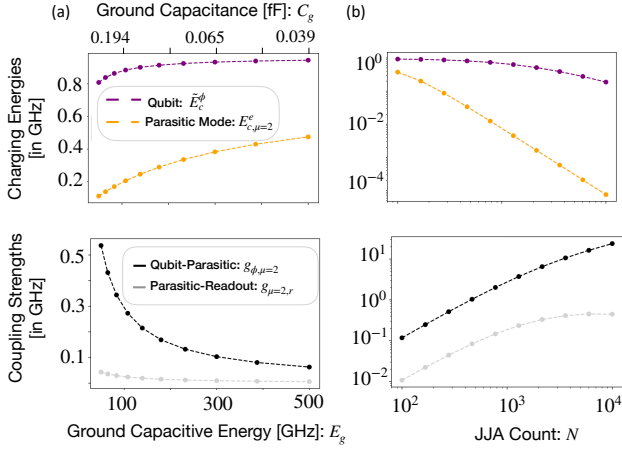


FIG. 14. The qubit charging energy in (a) decides the frequency and the parasitic charging energy in (b) decides the parasitic mode frequency. (c,d) give the plots for the coupling strengths of the parasitic mode to readout and qubit, respectively. All plots are obtained under linear JJA approximation. [SS: Add factor  $1/2\pi$  for the coupling strengths notations in the legend. Correct these plots]

### 3. Dispersive Hamiltonian

We use the Schrieffer-Wolff approximation to extract the readout parameters in Table. II, for example, dispersive shift of the qubit due to the parasitic modes  $\chi_{\phi\mu}$  and the readout mode  $\chi_{\phi r}$  [26] used to generate Fig. 6,

$$2\pi H = \frac{\omega_q}{2} \sigma_z + \sum_{\mu} (\omega_{\mu} + k_{\mu}) a_{\mu}^{\dagger} a_{\mu} + \omega_r a_r^{\dagger} a_r + \chi_{r,\phi} \sigma_z a_r^{\dagger} a_r + \sum_{\mu} \chi_{\mu,\phi} \sigma_z a_{\mu}^{\dagger} a_{\mu} + \sum_{\mu} \chi_{r\mu} a_{\mu}^{\dagger} a_{\mu} a_r^{\dagger} a_r \quad (B3)$$

$$= \frac{\omega_q}{2} \sigma_z + (\omega_r + \chi_{r\phi} \sigma_z) a_r^{\dagger} a_r + \sum_{\mu} (\omega_{\mu} + k_{\mu} + \chi_{r\mu} a_r^{\dagger} a_r + \chi_{\mu\phi} \sigma_z) a_{\mu}^{\dagger} a_{\mu} \quad (B4)$$

where  $\omega_q$  or  $\omega_{01} = \epsilon_0 - \epsilon_1$

$$+ |\langle 0|p_{\phi}|1\rangle|^2 \left[ 16g_{r\phi}^2 E_{C_r}^2 \sqrt{\frac{E_{L_r}}{32E_{C_r}}} \frac{2\epsilon_{01}}{\epsilon_{01}^2 - \omega_r^2} + \sum_{\mu} \left\{ g_{\mu\phi}^2 \sqrt{\frac{E_J^j}{32\tilde{E}_{C,\mu}^e}} \frac{2\epsilon_{01}}{\epsilon_{01}^2 - \omega_{\mu}^2} \right\} \right] + \sum_{l>1} 16g_{r\phi}^2 E_{C_r}^2 \sqrt{\frac{E_{L_r}}{32E_{C_r}}} \left[ \frac{|\langle 0|p_{\phi}|l\rangle|^2}{\epsilon_{0l} - \omega_r} - \frac{|\langle 1|p_{\phi}|l\rangle|^2}{\epsilon_{1l} - \omega_r} \right] + \sum_{l>1,\mu} \left\{ g_{\mu\phi}^2 \sqrt{\frac{E_J^j}{32\tilde{E}_{C,\mu}^e}} \times \left[ \frac{|\langle 0|p_{\phi}|l\rangle|^2}{\epsilon_{0l} - \omega_{\mu}} - \frac{|\langle 1|p_{\phi}|l\rangle|^2}{\epsilon_{1l} - \omega_{\mu}} \right] \right\} \quad (B5)$$

$$k_{\mu \in 2\mathbb{Z}} = 16E_{C_r}^2 \sqrt{\frac{E_{L_r}}{32E_{C_r}}} \sqrt{\frac{E_J^j}{32E_{C_r}^e}} \left[ \frac{g_{r\mu}^2}{\omega_{\mu} - \omega_r} \right] \leq \mathcal{O}(10^{-8}) \quad (B6)$$

$$\chi_{r,\phi} = 16g_{r\phi}^2 E_{C_r}^2 \sqrt{\frac{E_{L_r}}{32E_{C_r}}} \frac{2\epsilon_{01}}{\epsilon_{01}^2 - \omega_r^2} |\langle 0|p_{\phi}|1\rangle|^2 + 16g_{r\phi}^2 E_{C_r}^2 \sqrt{\frac{E_{L_r}}{32E_{C_r}}} \left[ \sum_l |\langle 0|p_{\phi}|l\rangle|^2 \frac{\epsilon_{0l}}{\epsilon_{0l}^2 - \omega_r^2} - \sum_l |\langle 1|p_{\phi}|l\rangle|^2 \frac{\epsilon_{1l}}{\epsilon_{1l}^2 - \omega_r^2} \right] \quad (B7)$$

$$\chi_{\mu,\phi} = g_{\mu\phi}^2 \sqrt{\frac{E_J^j}{32\tilde{E}_{C,\mu}^e}} \frac{2\epsilon_{01}}{\epsilon_{01}^2 - \omega_{\mu}^2} |\langle 0|p_{\phi}|1\rangle|^2 + g_{\mu\phi}^2 \sqrt{\frac{E_J^j}{32\tilde{E}_{C,\mu}^e}} \left[ \sum_l |\langle 0|p_{\phi}|l\rangle|^2 \frac{\epsilon_{0l}}{\epsilon_{0l}^2 - \omega_{\mu}^2} - \sum_l |\langle 1|p_{\phi}|l\rangle|^2 \frac{\epsilon_{1l}}{\epsilon_{1l}^2 - \omega_{\mu}^2} \right] \quad (\text{see Fig. 15}) \quad (B8)$$

Therefore  $\omega_q = -7e - 04$  GHz,  $\omega_{q,r} = -1.1e - 03$  GHz, see Fig. 15 for  $\omega_{q,\mu}, \chi_{\mu,\phi}$ .

The dispersive shift between the qubit and the readout is small due to the small charge matrix elements. The primary element which contributes to this quantity is the 03 and 12 charge matrix elements.

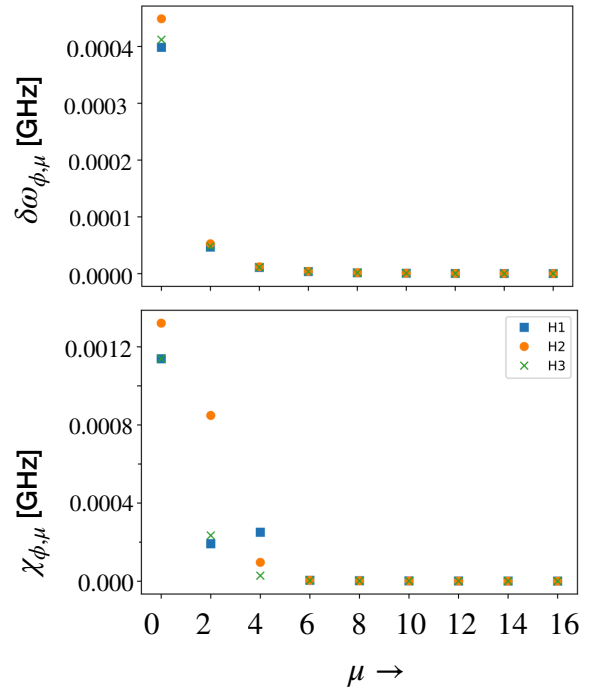


FIG. 15. All values are in  $\frac{\text{GHz}}{2\pi}$  units. The color code follows:  $H_1$  (blue),  $H_2$  (orange),  $H_3$  (green) for the three circuits shown in Fig. 14(a-c). (Top) Change in the qubit frequency due to parasitic mode  $\mu$  (Bottom) Dispersive shift  $\chi_{\mu}$  of the qubit concerning the parasitic mode  $\mu$ .

### Appendix C: Driven Fluxonium Circuit

Here, we will discuss the several analyses used in the driven fluxonium circuit including the semi-classical approximation and methods used in Sec. III to compute the readout efficiency. We first start with the derivation of  $H_{s.c.}$  in Eq. 4. [Derivation goes here](#)

#### 1. Approximations for Numerical Modelling

We use the following three approximations to make the problem at hand simpler

- Restriction to  $\mu = 2$ . We restrict our analyses to the closest even parasitic mode that couples most strongly to the qubit and the readout as evident from Fig. 14(d). This assumption helps us to lower bound the errors. Although it will be an interesting study to see if there are transitions caused due to higher modes that are more probable but in this work we aim at a proof of principle quantitative evidence of the presence of such transitions even with out modest assumptions.
- Semi-classical drive approximation. This approximation treats the readout resonator classically as described in Refs. [18–21] reducing one mode from our numerical simulation. This assumption is essential since unlike the case of transmon or fluxonium without collective modes, with all the above approximation, a full quantum simulation of the problem will still require three modes.
- Linear JJA Approximation. We assume that the parasitic modes behave as linear oscillators due to the large  $E_{J_j}/E_{C_j} = 200$  ratio. This approximation is explained in App. B. The non-linear corrections to our results, while essential, is beyond the scope of this work. For details on how nonlinear corrections affect different circuit parameters in play we direct the readers to Ref. [26]. Due to this assumption, we can use a Hilbert size of  $20 \times 3$  where only three levels are assumed in the linear parasitic mode subspace. In the presence of nonlinearity, the Hilbert size would need to be much larger to capture the required effects. Note that for the conclusions drawn in this paper, we are only interested in the presence of p-MIST effects and do not claim to quantify how many such transitions can be present. Hence, 3 levels in the parasitic mode are enough. In addition, we have verified that changing the truncation of the parasitic mode to 10 levels does not change the energy spacing.

[Here goes the truncation figure](#)

#### 2. Stark Shift

To observe a state transition the primary requirements are high charge matrix elements and low en-

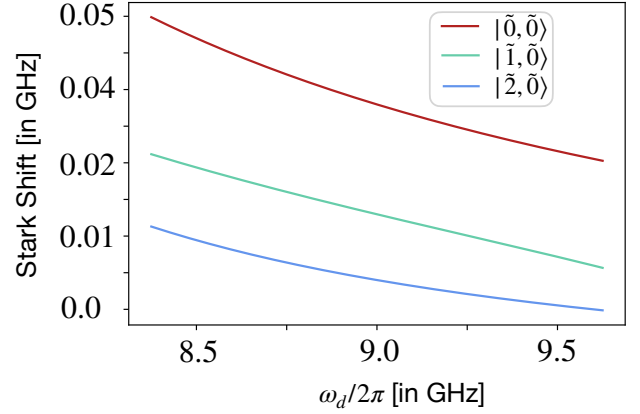


FIG. 16. Stark shift in different qubit levels under observation for readout computed using Eq. C1.

ergy difference. The eigen-energies of the states in question are changed with an increase in the number of readout photons or, in this case, the drive strength. So, in this section, we compute the stark shifted eigen-energies which can help in the prediction of an avoided crossing, given  $\bar{n}_r, \omega_r$  and the charge matrix elements. These stark shift formulas are used in the computing the probability of transitions using generalized Fermi's golden rule and Landau-Zener calculations. Let  $|i\rangle$  be a state in the eigenspace of  $H_{int} = H_\phi + H_{\mu=2} + g_{\phi\mu}\hat{N}_\phi\hat{N}_\mu$ . Following derivations in App. B the ac stark-shift in the energy of state  $|i\rangle$  at an average number of readout photons  $\bar{n}_r$  is given by,

$$\chi_i(\bar{n}_r) = 2\bar{n}_r \sum_f \omega_{if} \left[ \frac{g_{\phi r} |\langle i | \hat{N}_\phi | f \rangle|^2}{\omega_d^2 - \omega_{if}^2} + \frac{g_{\mu r} |\langle i | \hat{N}_\mu | f \rangle|^2}{\omega_d^2 - \omega_{if}^2} \right] \quad (C1)$$

Here  $\omega_{if} = E_f - E_i$  denote the energy difference in the eigen-energies of the  $|i\rangle$ . The impact due to the second term as expected is much smaller than the first term, and hence  $g_{\phi r}$  primarily governs this stark shift.

#### 3. Transition Rates and Quasienergies

Below we guess process responsible for each transition using first and second order fermi's golden rule calculations. We have computed rates using fermi's golden rule up to second order terms, as many of these transitions occur between a parity-conserving states, a forbidden first order transition. We compute these transitions involving up to 4 readout photons, as suggested by energy conservation. Under the same classical approximation, we can identify our parent Hamiltonian as  $H_0$  and perturbation  $V$  as follows,

$$H_0 = H_\phi + \omega_\mu \hat{a}_\mu^\dagger \hat{a}_\mu + g_{\phi,\mu} \hat{N}_\phi \hat{N}_\mu \quad (C2)$$

$$V = 2\sqrt{\bar{n}_r} (g_{r,\phi} \hat{N}_\phi + g_{r,\mu} \hat{N}_\mu) \sin \omega_d t, \quad (C3)$$

where  $\mu$  is the density of states which will be a Dirac Delta function in the absence of loss while it will be

Lorentzian in the presence of loss  $\frac{\kappa}{2\pi} = 50$ . In units of  $\hbar$  we have,

$$\Gamma_{i \rightarrow f} = |\langle f | H_1 | i \rangle|^2 \mu(E_i - E_f) \quad (\text{first-order}) \quad (C4)$$

$$= \sum_m \frac{|\langle f | H_1 | m \rangle \langle m | H_1 | i \rangle|^2}{|E_i - E_m - k\hbar\omega_d|^2} \mu(E_f - E_i - n\hbar\omega_d) \quad (\text{second-order}) \quad (C5)$$

We use a Lorentzian density of states at a  $\frac{\kappa}{2\pi} = 1.5$  KHz. Here  $k < n$  is used to compute the detuning with the intermediate state involved in the transition. Note that increasing the width of the Lorentzian  $\kappa$  resulting in an increase in the FG rates. Thus, here the decay rate does not yield any insights into the diabaticity at the transition, and hence the  $\kappa$  variation here is not the same as the  $\kappa$  variation in Sec. III B.

While these calculations include stark shifts in the energies of the states, we know that the first-order perturbative correction is not enough for some of the more higher states as seen in the comparisons of quasi-energies from Floquet simulations and predictions of stark shifted transitions. Thus, the computation below is only based on a heuristic developed from this approximate calculation. All transitions are computed at  $\bar{n}_r = 50$ . We note that the Fermi's golden rule calculations higher rates at the frequencies predicted by  $g_{\phi\mu} = 0$  case where the two frequencies are extremely different, for example, transitions 10 and 14. This happens since the Fermi's golden rule calculations are only approximately computing the stark-shifted energies for states which are more hybridized due to the presence of coupling  $g_{\phi\mu}$ . This behaviour is evident in Figs. 17, 18, 19. We will compare the considerable FG rates with well-separated quasi-energy gap at the avoided crossings  $\Delta_{ac}$  seen in these figures.

For the case of  $|i\rangle = |0, 0\rangle$  shown in Fig. 17, we quote the rates for each process and state how many readout photons were involved, guess the possible intermediate state and whether it could be a first- or second-order process. This heuristic analysis is still interesting since it helps us understand the processes involved behind general MIST processes and p-MIST processes, identifying any unique feature or extremely high rates, if so.

- 1 This is a first order transition involving three readout photons ( $3r$ ) which yields a Fermi's golden rule rate of 40 KHz.
- 2 The first process is a second-order process which absorbs two photons ( $2r$ ) through an intermediate state with energy close to  $E_i + \omega_r$  at a rate of 4 MHz where  $\Delta_{ac} = 4$  MHz. The second process is a second-order which absorbs four photons ( $4r$ ) through an intermediate state close to  $E_i + 3\omega_r$  at a rate of 22 KHz.
- 3 This is a Rabi transition involving a virtual state via a second-order two-photon process ( $2r$ ) at a rate of 0.028 KHz.
- 4-6 The first transition is a second order two-photon process  $2r$  with an FG rate of 1.26 KHz at  $\omega_r = 9.36$  GHz. The second process is a Rabi transition at a rate of 10 KHz.

Next, we look at the transition rates for the  $|\tilde{0}, \tilde{1}\rangle$ , the state involved in the computation as well as readout in a low-frequency fluxonium, shown in Fig. 18.

- 7 This is a second order process involving four readout photons ( $4r$ ) at a rate of 21 KHz. The intermediate state involved is close to a frequency of  $E_i + 3\omega_r$ .
- 8 This is a second order process involving two readout photons ( $2r$ ) with a transition rate of 45 KHz. The energy gap at the avoided crossing for this transition is less than 1 MHz.
- 9 This is a second order process involving four readout  $4r$  photons occurring at a rate of 0.95 KHz, where the intermediate state energy is close to  $E_i + 3\omega_r$ .
- 10 This is a second order process involving two readout  $2r$  photons occurring at a rate of 91 KHz. Fig. 5 also confirms that the transition 9 occurs with a higher probability compared to transition 8. The energy gap at the avoided crossing is
- 11 This is a first order process involving three readout photons ( $3r$ ) occurring at a rate of 2.2 KHz.
- 12 This is a second order process involving two readout photons ( $2r$ ) occurring at a rate of 52 KHz where  $\Delta_{ac} = 1.1$  MHz.

Finally, we look at the transition rates for the  $|\tilde{0}, \tilde{2}\rangle$ , the state involved in the readout of a low-frequency fluxonium, shown in Fig. 19.

- 13 This is a second order process involving two-readout photons ( $2r$ ) occurring at a rate of 16 (1) MHz which is the same as  $\Delta_{ac}$ .
- 14 This is a second order process involving two-readout photons ( $2r$ ) occurring at a rate of 2.2 KHz.
- 15 The first process is first order while the second process is second order, both involving ( $1r$ ) and ( $2r$ ) readout photons. The rates of these transitions are 1.48 KHz and 28 KHz, respectively. The energy gap at this avoided crossing is 4 MHz. Thus, this transition appears to be either a higher order process or a weaker transition.

#### 4. Landau-Zener Probabilities

We compute the Landau-Zener probabilities numerically using the quasienergies from the Floquet simulations and analytically using the stark-shifted eigenenergies. In order to convert the Floquet simulation used with variation in  $\bar{n}_r$  at a fixed time  $t$  (ignoring the short scale fast dynamics over a time period), in this case, we will use a time-dependent case where  $\bar{n}_r$  varies as  $\bar{n}_r = 50(1 - e^{-\kappa T/2})^2$  to emulate change in



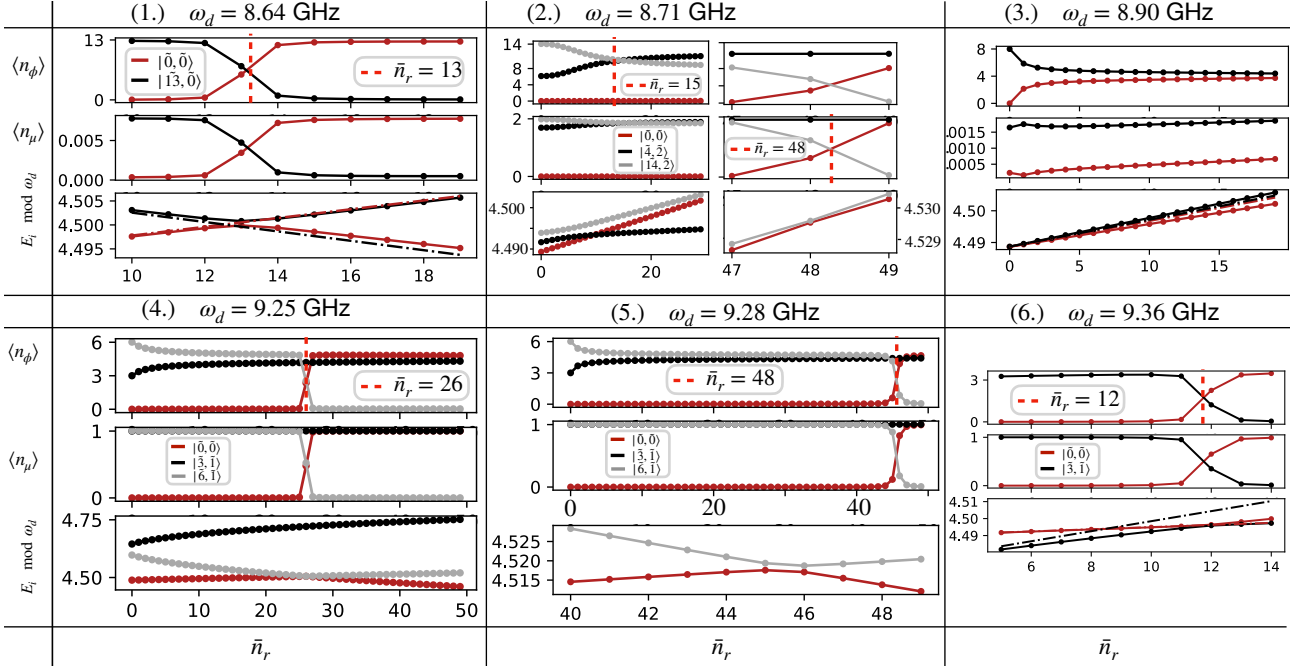


FIG. 17. MIST effects from Table III involving the  $|\tilde{0}, \tilde{0}\rangle$  state. (Top row) Fluxonium subspace  $\langle n_\phi \rangle$ . (Middle) Parasitic mode subspace  $\langle n_\mu \rangle$  (Bottom) Stark-shifted eigen-energies (dashed) and quasi-energies (solid) from Floquet simulations, corresponding to the initial state  $i$  as per the legend. Inset shows avoided crossing of quasi-energies. Floquet results are extracted from numerical data used for Fig. 3.

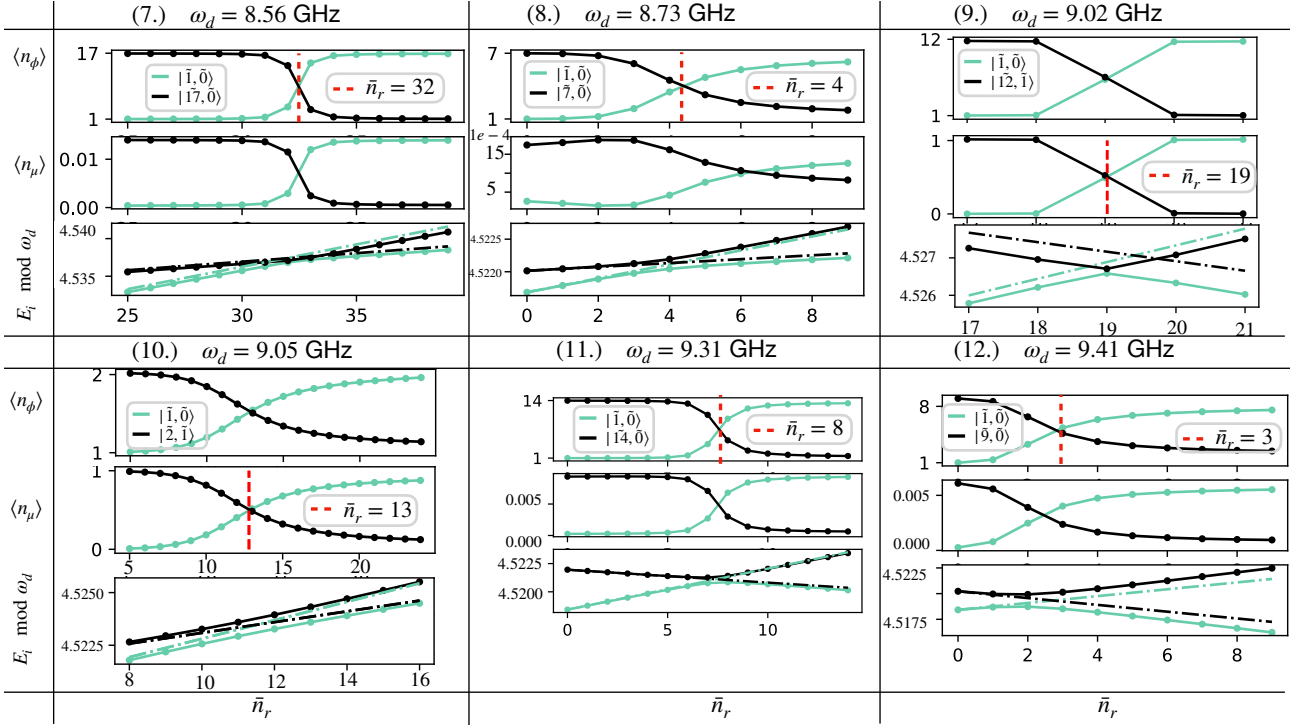


FIG. 18. MIST effects from Table III involving the  $|\tilde{1}, \tilde{0}\rangle$  state. (Top row) Fluxonium subspace  $\langle n_\phi \rangle$ . (Middle) Parasitic mode subspace  $\langle n_\mu \rangle$  (Bottom) Stark-shifted eigen-energies (dashed) and quasi-energies (solid) from Floquet simulations, corresponding to the initial state  $i$  as per the legend. Inset shows avoided crossing of quasi-energies. Floquet results are extracted from numerical data used for Fig. 3.

readout photons from dissipation. The numerical calculations use the probability for Landau-Zener transitions given in [28] for an avoided crossing observed

between states  $i, f$ ,

$$P_{LZ} = \exp \left[ -\pi \frac{\Delta_{ac}^2}{2v} \right], \quad (C6)$$

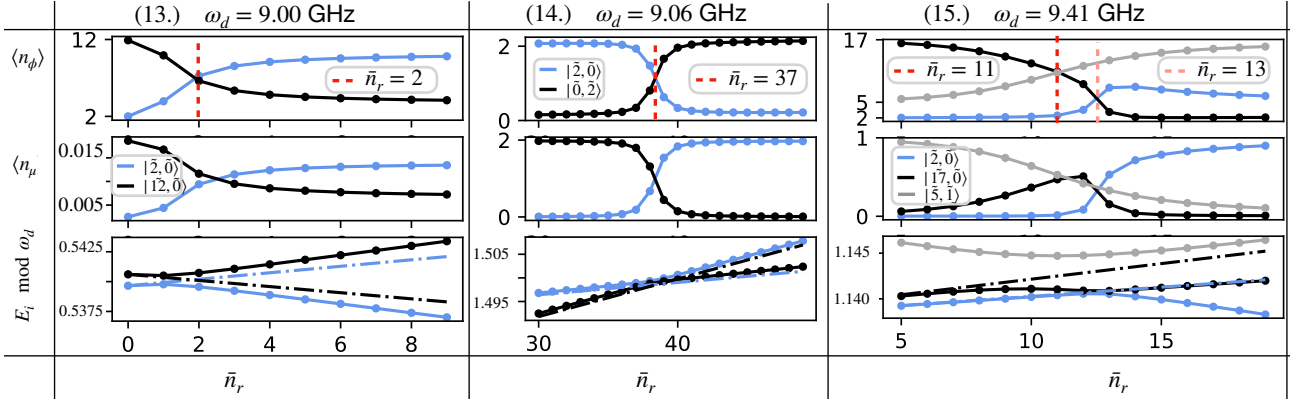


FIG. 19. MIST effects from Table III involving the  $|\tilde{2}, \tilde{0}\rangle$  state. (Top row) Fluxonium subspace  $\langle n_\phi \rangle$ . (Middle) Parasitic mode subspace  $\langle n_\mu \rangle$  (Bottom) Stark-shifted eigen-energies (dashed) and quasi-energies (solid) from Floquet simulations, corresponding to the initial state  $i$  as per the legend. Inset shows avoided crossing of quasi-energies. Floquet results are extracted from numerical data used for Fig. 3.

$$\text{where } v = \sqrt{2\Delta_{ac} \left| \frac{d^2 \epsilon_f}{d\bar{n}_r(t)^2} \right|_{t_{ac}} \frac{d\bar{n}_r(t)}{dt} \Big|_{t_{ac}}} \quad (\text{C7})$$

Here, the variable  $\epsilon_j$  is the numerically computed quasi-energy obtained from Floquet simulations, while  $\Delta_{ac}$  refers to the quasi-energy difference at avoided crossing.

For the analytical calculations, we use the well-known formula (with energy in units of GHz),

$$P_{LZ} = \exp \left[ -4\pi^2 \frac{V}{\frac{\partial \omega_{if}}{\partial \bar{n}_r(t)} \frac{d\bar{n}_r(t)}{dt}} \right], \quad (\text{C8})$$

$$\text{where } V = |\langle i | H_t | f \rangle|^2 \quad (\text{C9})$$

$$\omega_{if} = E_f + \chi_f(\bar{n}_r(t)) - E_i - \chi_i(\bar{n}_r(t)) \quad (\text{C10})$$

Here  $\chi_i(\bar{n}_r(t)), \chi_f(\bar{n}_r(t))$  are ac stark shifts in the eigen-energies of  $i, j$  due to  $\bar{n}_r$  average readout photons. See app. C2 for the calculation of these quantities.

## 5. Parasitic Dephasing due to Thermal Effects

In this appendix, we lay out in detail our calculations of dephasing induced by the random occupation of the parasitic modes due to thermal effects. We assume a scenario where the circuit is connected to a bath at  $0K$  such that thermal photons can be set to  $n_{th} = 0$ . The parasitic mode is randomly populated to some non-zero  $\bar{n}_\mu$  induced by the coupling of the readout with the parasitic mode. Now, at some point this population will go back to  $\bar{n}_\mu = 0$  due to the decay of the parasitic modes dominated by the rate  $\kappa_\mu = \frac{\omega_\mu}{Q_\mu}$ . Here  $Q_\mu, \omega_\mu$  are the quality factor and frequency of the parasitic mode. We are set to compute the dephasing due to the fluctuation in this quantity as the parasitic mode decays. We can compute the total decay rate of the parasitic modes as follows [42],

$$k_\mu = \kappa_r \frac{g_{\mu,r}^2}{\Delta^2} + \frac{\omega_\mu}{Q_\mu}, \quad (\text{C11})$$

where  $\Delta$  is the detuning between the parasitic mode frequency and the readout drive frequency. The first

terms and second terms depict contributions from Purcell effect due to the readout resonator ( $\approx \text{Hz}$ ) and the quality factor  $Q_\mu$  of the parasitic modes ( $\approx \text{KHz-MHz}$ ). The second term dominates the expression and will determine the decay rate of the parasitic modes.

In this context, we use the methods described in Ref. [43] to compute the dephasing of a qubit given the initial occupation of the parasitic mode and the strong coupling between the qubit and the parasitic mode. Here, we use the dispersive Hamiltonian (see Eq. B4) of qubit-parasitic mode system, without the readout. This assumption on the system is well-suited to cases where measurement has populated the parasitic mode. In the absence of any state transition in the fluxonium circuit, the parasitic mode is populated to  $\bar{n}_\mu = \mathcal{O}(10^{-4})$  as shown in Fig. 7(a) due to the readout-parasitic mode coupling.

$$\frac{H}{\hbar} = \frac{\omega_q}{2} \sigma_z + \sum_\mu \left( \omega_\mu + k_\mu + \chi_{\mu\phi} \sigma_z \right) a_\mu^\dagger a_\mu, \quad (\text{C12})$$

$$+ \xi_{\mu r} \hat{N}_\phi \sin \omega_d t \quad (\text{C13})$$

where,  $\kappa_\mu$  is the lamb shift,  $\chi_\mu$  is the stark shift, and  $\omega_\mu$  is the frequency of the parasitic mode. The variable  $\omega_q$  denotes the qubit frequency i.e. the energy gap between the ground and the first excited state of the qubit potential. We ignore the qubit drive in this case since it will not play a role in the question of concern. In the presence of a qubit coupling, the state transitions will dominate the lifetimes and thus calculation of dephasing rates takes a backseat. In this scenario we are in the weak damping, strong coupling limit as  $g_{\mu\phi}$  is of the order of GHz while the damping  $\kappa_\mu = \frac{\omega_\mu}{Q_\mu}$  is of the order of MHz or KHz since all parasitic modes are designed to be high  $Q$  cavities. In the limit of zero temperature Ref. [43] shows that the dephasing rate coincides with what has been found in Ref. [42]. We use the calculations for the dispersive Hamiltonian (see Eq. B4 in App. B) to calculate for the drive-dependent dephasing rate at zero temperature quoted in [42, 43] assuming an initial  $\bar{n}_r$ .

$$\Gamma_\theta = \sum_\mu \frac{1}{2} \frac{|\xi_{\mu,r}|^2 \chi_{\mu,\phi}^2 \kappa_\mu}{[(\Delta + \chi_{\mu,\phi})^2 + (\kappa_\mu/2)^2]} \times \frac{1}{[(\Delta - \chi_{\mu,\phi})^2 + (\kappa_\mu/2)^2]} \quad (\text{C14})$$

$$= \sum_\mu \left[ \frac{\chi_{\mu,\phi}^2 \kappa_\mu}{\Delta^2 + \kappa^2/4 + \chi_{\mu,\phi}^2} \right] \bar{n}_\mu, \quad (\text{C15})$$

The thermal population of the parasitic modes is capped at  $10^{-3}$  for  $T = 50mK$  (see App. B) inducing a dephasing rate of  $\Gamma_\phi = 10^{-6}$  GHz.

#### Appendix D: Alternative Circuit

Here goes the details on Will Oliver's parameters and figures for coupling strengths etc.

- 
- [1] [Phys. Rev. X 9, 041041 \(2019\) - High-Coherence Fluxonium Qubit \(2019\)](#).
  - [2] A. Somoroff, Q. Ficheux, R. A. Mencia, H. Xiong, R. Kuzmin, and V. E. Manucharyan, Millisecond Coherence in a Superconducting Qubit, [Physical Review Letters 130, 267001 \(2023\)](#), publisher: American Physical Society.
  - [3] [Fluxonium: Single Cooper-Pair Circuit Free of Charge Offsets | Science \(2009\)](#).
  - [4] N. Earnest, S. Chakram, Y. Lu, N. Irons, R. K. Naik, N. Leung, L. Ocola, D. A. Czaplewski, B. Baker, J. Lawrence, J. Koch, and D. I. Schuster, Realization of a  $\mathbb{Z}_2$  System with Metastable States of a Capacitively Shunted Fluxonium, [Physical Review Letters 120, 150504 \(2018\)](#), publisher: American Physical Society.
  - [5] H. Zhang, S. Chakram, T. Roy, N. Earnest, Y. Lu, Z. Huang, D. Weiss, J. Koch, and D. I. Schuster, Universal fast flux control of a coherent, low-frequency qubit, [Physical Review X 11, 011010 \(2021\)](#), arXiv:2002.10653 [cond-mat, physics:quant-ph].
  - [6] L. Ding, M. Hays, Y. Sung, B. Kannan, J. An, A. Di Paolo, A. H. Karamlou, T. M. Hazard, K. Azar, D. K. Kim, B. M. Niedzielski, A. Melville, M. E. Schwartz, J. L. Yoder, T. P. Orlando, S. Gustavsson, J. A. Grover, K. Serniak, and W. D. Oliver, High-Fidelity, Frequency-Flexible Two-Qubit Fluxonium Gates with a Transmon Coupler, [Physical Review X 13, 031035 \(2023\)](#), publisher: American Physical Society.
  - [7] H. Zhang, C. Ding, D. Weiss, Z. Huang, Y. Ma, C. Guinn, S. Sussman, S. P. Chitta, D. Chen, A. A. Houck, J. Koch, and D. I. Schuster, Tunable Inductive Coupler for High-Fidelity Gates Between Fluxonium Qubits, [PRX Quantum 5, 020326 \(2024\)](#), publisher: American Physical Society.
  - [8] K. N. Nesterov, C. Wang, V. E. Manucharyan, and M. G. Vavilov, cnot Gates for Fluxonium Qubits via Selective Darkening of Transitions, [Physical Review Applied 18, 034063 \(2022\)](#), publisher: American Physical Society.
  - [9] K. N. Nesterov, Q. Ficheux, V. E. Manucharyan, and M. G. Vavilov, Proposal for Entangling Gates on Fluxonium Qubits via a Two-Photon Transition, [PRX Quantum 2, 020345 \(2021\)](#), publisher: American Physical Society.
  - [10] E. Dogan, D. Rosenstock, L. Le Guevel, H. Xiong, R. A. Mencia, A. Somoroff, K. N. Nesterov, M. G. Vavilov, V. E. Manucharyan, and C. Wang, Two-Fluxonium Cross-Resonance Gate, [Physical Review Applied 20, 024011 \(2023\)](#), publisher: American Physical Society.
  - [11] E. L. Rosenfeld, C. T. Hann, D. I. Schuster, M. H. Ma-theny, and A. A. Clerk, Designing high-fidelity two-qubit gates between fluxonium qubits, arXiv preprint arXiv:2403.07242 (2024).
  - [12] [PRX Quantum 3, 037001 \(2022\) - Blueprint for a High-Performance Fluxonium Quantum Processor \(2022\)](#).
  - [13] N. A. Masluk, I. M. Pop, A. Kamal, Z. K. Mineev, and M. H. Devoret, Microwave Characterization of Josephson Junction Arrays: Implementing a Low Loss Superinductance, [Physical Review Letters 109, 137002 \(2012\)](#), publisher: American Physical Society.
  - [14] F. Wang, K. Lu, H. Zhan, L. Ma, F. Wu, H. Sun, H. Deng, Y. Bai, F. Bao, X. Chang, *et al.*, Achieving millisecond coherence fluxonium through overlap josephson junctions, arXiv preprint arXiv:2405.05481 (2024).
  - [15] D. G. Ferguson, A. A. Houck, and J. Koch, Symmetries and collective excitations in large superconducting circuits, [Physical Review X 3, 011003 \(2013\)](#).
  - [16] A. Blais, A. L. Grimsmo, S. M. Girvin, and A. Wallraff, Circuit quantum electrodynamics, [Reviews of Modern Physics 93, 025005 \(2021\)](#).
  - [17] R. Shillito, A. Petrescu, J. Cohen, J. Beall, M. Hauru, M. Ganahl, A. G. Lewis, G. Vidal, and A. Blais, Dynamics of transmon ionization, [Physical Review Applied 18, 034031 \(2022\)](#).
  - [18] X. Xiao, J. Venkatraman, R. G. Cortiñas, S. Chowdhury, and M. H. Devoret, A diagrammatic method to compute the effective hamiltonian of driven nonlinear oscillators, arXiv preprint arXiv:2304.13656 (2023).
  - [19] M. Khezri, A. Opremcak, Z. Chen, K. C. Miao, M. McEwen, A. Bengtsson, T. White, O. Naaman, D. Sank, A. N. Korotkov, *et al.*, Measurement-induced state transitions in a superconducting qubit: Within the rotating-wave approximation, [Physical Review Applied 20, 054008 \(2023\)](#).
  - [20] J. Cohen, A. Petrescu, R. Shillito, and A. Blais, Reminiscence of classical chaos in driven transmons, [PRX Quantum 4, 020312 \(2023\)](#).
  - [21] M. F. Dumas, B. Groleau-Paré, A. McDonald, M. H. Muñoz-Arias, C. Lledó, B. D'Anjou, and A. Blais, Unified picture of measurement-induced ionization in the transmon, arXiv preprint arXiv:2402.06615 (2024).
  - [22] D. Sank, Z. Chen, M. Khezri, J. Kelly, R. Barends, B. Campbell, Y. Chen, B. Chiaro, A. Dunsworth, A. Fowler, *et al.*, Measurement-induced state transitions in a superconducting qubit: Beyond the rotating wave approximation, [Physical review letters 117, 190503 \(2016\)](#).
  - [23] K. N. Nesterov and I. V. Pechenezhskiy, Measurement-induced state transitions in dispersive qubit readout schemes, arXiv preprint arXiv:2402.07360 (2024).

- [24] L. B. Nguyen, Y.-H. Lin, A. Somoroff, R. Mencia, N. Grabon, and V. E. Manucharyan, High-coherence fluxonium qubit, *Physical Review X* **9**, 041041 (2019).
- [25] V. E. Manucharyan, J. Koch, L. I. Glazman, and M. H. Devoret, Fluxonium: Single cooper-pair circuit free of charge offsets, *Science* **326**, 113 (2009).
- [26] G. Viola and G. Catelani, Collective modes in the fluxonium qubit, *Physical Review B* **92**, 224511 (2015).
- [27] D. Gusenkova, M. Spiecker, R. Gebauer, M. Willsch, D. Willsch, F. Valenti, N. Karcher, L. Grünhaupt, I. Takmakov, P. Winkel, *et al.*, Quantum nondemolition dispersive readout of a superconducting artificial atom using large photon numbers, *Physical Review Applied* **15**, 064030 (2021).
- [28] T. N. Ikeda, S. Tanaka, and Y. Kayanuma, Floquet-landau-zener interferometry: Usefulness of the floquet theory in pulse-laser-driven systems, *Physical Review Research* **4**, 033075 (2022).
- [29] A relatively high-frequency choice, to reduce thermal, photon shot-noise induced dephasing in the qubit compared to lower-frequency bands.
- [30] G. Zhu, D. G. Ferguson, V. E. Manucharyan, and J. Koch, Circuit QED with fluxonium qubits: Theory of the dispersive regime, *Physical Review B* **87**, 024510 (2013), publisher: American Physical Society.
- [31] N. A. Masluk, *Reducing the losses of the fluxonium artificial atom* (Yale University, 2013).
- [32] A. G. Fowler, M. Mariantoni, J. M. Martinis, and A. N. Cleland, Surface codes: Towards practical large-scale quantum computation, *Physical Review A—Atomic, Molecular, and Optical Physics* **86**, 032324 (2012).
- [33] L. Ding, M. Hays, Y. Sung, B. Kannan, J. An, A. Di Paolo, A. H. Karamlou, T. M. Hazard, K. Azar, D. K. Kim, *et al.*, High-fidelity, frequency-flexible two-qubit fluxonium gates with a transmon coupler, *Physical Review X* **13**, 031035 (2023).
- [34] S. Hazra, W. Dai, T. Connolly, P. Kurilovich, Z. Wang, L. Frunzio, and M. Devoret, Benchmarking the readout of a superconducting qubit for repeated measurements, *arXiv preprint arXiv:2407.10934* (2024).
- [35] Z. Huang, P. S. Mundada, A. Gyenis, D. I. Schuster, A. A. Houck, and J. Koch, Engineering dynamical sweet spots to protect qubits from  $1/f$  noise, *Phys. Rev. Appl.* **15**, 034065 (2021).
- [36] M. D. Reed, L. DiCarlo, B. R. Johnson, L. Sun, D. I. Schuster, L. Frunzio, and R. J. Schoelkopf, High-Fidelity Readout in Circuit Quantum Electrodynamics Using the Jaynes-Cummings Nonlinearity, *Physical Review Letters* **105**, 173601 (2010), publisher: American Physical Society.
- [37] M. H. Muñoz-Arias, C. Lledó, and A. Blais, Qubit readout enabled by qubit cloaking, *Physical Review Applied* **20**, 054013 (2023), publisher: American Physical Society.
- [38] N. Didier, J. Bourassa, and A. Blais, Fast Quantum Nondemolition Readout by Parametric Modulation of Longitudinal Qubit-Oscillator Interaction, *Physical Review Letters* **115**, 203601 (2015), publisher: American Physical Society.
- [39] G. Catelani, R. J. Schoelkopf, M. H. Devoret, and L. I. Glazman, Relaxation and frequency shifts induced by quasiparticles in superconducting qubits, *Physical Review B* **84**, 064517 (2011).
- [40] J. Koch, V. Manucharyan, M. Devoret, and L. Glazman, Charging effects in the inductively shunted josephson junction, *Physical review letters* **103**, 217004 (2009).
- [41] Alternatively, for the coupling strengths with readout, we multiply with the constant factor of  $\frac{1}{2\pi}\omega_r\sqrt{\frac{\pi Z}{R_k}} \approx 1$  in GHz for (eV/h), where  $R_k = h/e^2 = 25.8K\Omega$ ,  $Z = 50 * 4/\pi\Omega$ ,  $\omega_r \approx 10\text{GHz}$ . Thus,  $eVZPF/h = 0.14$  which can be checked against  $n_{ZPF,r}$  quoted for chip 2(A&B) as follows.  $n = Q/2e = CV/2e = (eV/h)/\omega_r * Z_r * 2e^2/h = 0.14/(2\omega_r * Z_r/R_k) = 2.84$ .
- [42] J. Gambetta, A. Blais, D. I. Schuster, A. Wallraff, L. Frunzio, J. Majer, M. H. Devoret, S. M. Girvin, and R. J. Schoelkopf, Qubit-photon interactions in a cavity: Measurement-induced dephasing and number splitting, *Physical Review A* **74**, 042318 (2006).
- [43] A. Clerk and D. W. Utami, Using a qubit to measure photon-number statistics of a driven thermal oscillator, *Physical Review A—Atomic, Molecular, and Optical Physics* **75**, 042302 (2007).